Quantifying diapir ascent velocities in power-law viscous rock under far-field stress: Integrating analytical estimates, 3D numerical calculations and geodynamic applications

Emilie Macherel[1], Yuri Podladchikov[1], Ludovic Räss[2,3], and Stefan M. Schmalholz[1]

[1]University of Lausanne, ISTE, Lausanne, Switzerland
[2]Laboratory of Hydraulics, Hydrology and Glaciology (VAW), ETH Zurich, Switzerland
[3]Swiss Federal Institute for Forest, Snow and Landscape Research (WSL), Birmensdorf, Switzerland

Key Points:

- 3D GPU-based numerical calculations of diapir velocities in power-law viscous fluid under horizontal simple shear
- New analytical velocity estimates are controlled by two stress ratios and agree with numerical results
- Stress weakening in tectonically active regions can increase diapir velocity by several orders of magnitudes

Corresponding author: Emilie Macherel, emilie.macherel@unil.ch

Abstract

Diapirism is crucial for heat and mass transfer in many geodynamic processes. Understanding diapir ascent velocity is vital for assessing its significance in various geodynamic settings. Although analytical estimates exist for ascent velocities of diapirs in power-law viscous, stress weakening fluids, they lack validation through 3D numerical calculations. Here, we improve these estimates by incorporating combined linear and power-law viscous flow and validate them using 3D numerical calculations. We focus on a weak, buoyant sphere in a stress weakening fluid subjected to far-field horizontal simple shear. The ascent velocity depends on two stress ratios: (1) the ratio of buoyancy stress to characteristic stress, controlling the transition from linear to power-law viscous flow, and (2) the ratio of regional stress associated with far-field shearing to characteristic stress. Comparing analytical estimates with numerical calculations, we find analytical estimates are accurate within a factor of two. However, discrepancies arise due to the analytical assumption that deviatoric stresses around the diapir are comparable to buoyancy stresses. Numerical results reveal significantly smaller deviatoric stresses. As deviatoric stresses govern stress-dependent, power-law, viscosity analytical estimates tend to overestimate stress weakening. We introduce a shape factor to improve accuracy. Additionally, we determine characteristic stresses for representative mantle and lower crustal flow laws and discuss practical implications in natural diapirism, such as sediment diapirs in subduction zones, magmatic plutons or exhumation of ultra-high-pressure rocks. Our study enhances understanding of diapir ascent velocities and associated stress conditions, contributing to a thorough comprehension of diapiric processes in geology.

Plain Language Summary

A diapir is a volume of rock that rises within a larger, denser rock mass due to its lower density and the force of gravity. Understanding the speed at which diapirs ascend is crucial for determining their significance in specific geologic settings, such as subduction zones. In this study, we use advanced computer simulations to calculate the ascent velocity of a spherical diapir within a denser surrounding material. The surrounding material is subjected to horizontal shearing, and its behaviour resembles that of a nonlinear fluid, where its resistance to shear, known as viscosity, depends on the applied stress. By conducting three-dimensional computer simulations, we not only test the accuracy of existing mathematical equations commonly used to estimate diapir velocity but also

make improvements to enhance their precision. These equations help us estimate how quickly diapirs rise in different geodynamic environments. By advancing our understanding of diapir ascent velocities, we gain valuable insights into the processes that shape our planet's geological features.

1 Introduction

Diaprism is an important mechanism of heat and mass transport in the Earth (e.g. Ramberg, 1968; Schubert et al., 2001; Turcotte & Schubert, 2021; Whitehead Jr. & Luther, 1975). It mainly occurs in viscously deforming rock (e.g. Turcotte & Schubert, 2021), but can also be initiated in settings with frictional overburden (e.g. Poliakov et al., 1993, 1996). Diapirism can occur on various temporal and spatial scales and is a mechanism for the ascent of, for example, magma, (e.g. Marsh, 1982; Cruden, 1988; Michail et al., 2021; Miller & Paterson, 1999; Rabinowicz et al., 1987; Weinberg & Podladchikov, 1994, 1995; Burov et al., 2003; Cruden & Weinberg, 2018), rock salt (e.g. Jackson et al., 1990; Jackson & Vendeville, 1994; Schultz-Ela et al., 1993; Poliakov et al., 1993), mud (e.g. Mazzini et al., 2009) or sediments buried at subduction zones (e.g. Klein & Behn, 2021; Marschall & Schumacher, 2012; Smye & England, 2023; Behn et al., 2011; Gerya & Yuen, 2003). Magma ascent by diapirism is, for example, an important mechanism contributing to the volcanic and igneous plumbing systems (e.g. Cruden & Weinberg, 2018). At subduction zones, for example, sediment diapirs, which detach from subducting slabs and rise into the above, hotter mantle wedge, are presumably the reason for the so-called sediment melt signature in arc lavas (e.g. Plank & Langmuir, 1993; Behn et al., 2011). Furthermore, diaprism was suggested as potential mechanism for the exhumation of some high- and ultra-high-pressure, (U)HP, terranes, for which very fast, > 1 cm/yr, exhumation velocities have been estimated (e.g. Burov et al., 2001, 2014; Little et al., 2011; Schmalholz & Schenker, 2016; Schwarzenbach et al., 2021). For all the various forms of diapirism, the ascent velocity of the diapir is the essential quantity to assess the importance of diapirism for specific geodynamic settings.

The simplest estimate for the ascent velocity of a diapir is given by the so-called Stokes law which is applicable for the ascent, or fall, of a rigid sphere in a denser, or lighter, linear viscous fluid (Stokes, 1850). However, diapirs in geodynamics are mostly not rigid and are commonly mechanically weaker than the surrounding rocks (e.g. Weinberg & Podladchikov, 1994). Furthermore, viscous deformation of natural rock surrounding a

rising diapir can occur by dislocation creep, which is described by a non-linear, power-law viscous flow flaw (e.g. Weinberg & Podladchikov, 1994). In a power-law viscous fluid, the effective viscosity depends on the stress, or alternatively the strain rate, in the fluid (e.g. Fletcher, 1974; Turcotte & Schubert, 2021; Schmalholz & Fletcher, 2011). For rocks, higher stresses cause smaller effective viscosities (e.g. Hirth & Kohlstedt, 2003; Karato, 2008). Here, we refer to the decrease of the effective viscosity caused by an increase in stress as stress weakening (e.g. Christensen, 1983). For diapirism, there are two fundamental mechanisms by which the stress, and hence the effective viscosity, in rocks surrounding a diapir can change (Figure 1): (1) The rock unit in which the diapir is rising undergoes a far-field deformation, for example due to horizontal simple shear in a strike-slip environment (e.g. Michail et al., 2021; Nahas et al., 2023) or corner flow in a mantle wedge (e.g. Klein & Behn, 2021). The far-field, or regional, stresses associated with the regional deformation can modify the effective viscosity of the rocks surrounding the diapir. (2) The deformation in the surrounding rocks, caused by the rising diapir, generates stress variations around the diapir (e.g. Weinberg & Podladchikov, 1994). Such local stress variations around the diapir are related to the diapir's buoyancy stress and cause variations in the effective viscosity of the surrounding rock.

Analytical estimates of the ascent velocity of a diapir in a power-law viscous fluid have been presented by Weinberg and Podladchikov (1994). Weinberg and Podladchikov (1994) show that the reduction of the effective viscosity due to local stress weakening is essential for magma diapirs to be able to ascent with velocities of 10 to 100 m/yr. Such high velocities are needed so that magma diapirs can reach the upper crust before solidification. Similar high velocities have been suggested for the rise of sediment diapirs across the mantle wedge, also enabled by stress weakening in power-law viscous mantle rocks (Klein & Behn, 2021). High velocities due to stress weakening in power-law viscous material are supported by two-dimensional (2D) numerical simulations of mantle convection (e.g. Larsen & Yeun, 1997). However, the analytical estimates derived by Weinberg and Podladchikov (1994) have never been tested and compared to results of full 3D numerical calculations.

Here, we perform full 3D numerical calculations to quantify the ascent velocity of a weak diapir in a stronger and deforming fluid. The flow law of the surrounding fluid is a combination of linear and power-law viscous flow. Such combined flow law can describe rock deformation by a combination of diffusion and dislocation creep (e.g. Karato,

2008). Our numerical algorithm is based on the staggered finite difference method and employs an iterative solution strategy. We programmed the algorithm in the Julia language and use GPUs for the numerical solution. In the numerical calculations, we consider effective viscosity variations in the surrounding fluid due to both regional stresses and local stress variations around the diapir. The regional stresses are caused by strike-slip shearing and the local stresses are caused by the upward movement of the diapir. We further elaborate the analytical estimates of Weinberg and Podladchikov (1994) by (i) implementing a combined linear and power-law viscous flow law, and (ii) considering both regional tectonic stress and local buoyancy stress. We then compare the analytical estimates with the 3D numerical calculations.

The aims of our study are to (i) elaborate, test and improve analytical estimates for diapiric ascent velocities in a deforming power-law viscous fluid, (ii) make a systematic quantification of the ascent velocity based on two dimensionless stress ratios and (iii) discuss the applicability of the results to typical crustal and mantle flow laws as well as to various diapir scenarios.

2 Model

2.1 Flow law and effective viscosity

We consider a non-linear, power-law viscous flow law of the general form (Fletcher, 1974; Karato, 2008):

$$\dot{\epsilon} = \frac{1}{2} B \tau^n \ , \tag{1}$$

with $\dot{\epsilon}$ being the deviatoric strain rate, τ being the deviatoric stress, n being the power-law stress exponent and B being a material parameter. We reformulate Equation (1) to:

$$\tau \ = \ 2B^{-1} \tau^{(1-n)} \dot{\epsilon} \ . \tag{2}$$

Next, we multiply the right-hand side of the Equation 2 by $\tau_{\mathrm{C}}^{(1-n)}/\tau_{\mathrm{C}}^{(1-n)}$, with τ_{C} being a characteristic stress magnitude, and rearrange Equation 2 to:

$$\tau = 2\eta \left(\frac{\tau}{\tau_{\mathrm{C}}} \right)^{(1-n)} \dot{\epsilon} \ , \tag{3}$$

where $\eta = B^{-1} \tau_{\mathrm{C}}^{(1-n)}$. Introducing the characteristic stress τ_{C} has two benefits: (1) The parameter η has units of a viscosity, i.e. Pa·s, and (2) the impact of τ on the flow law is normalized by the magnitude of τ_{C}. The additional usefulness of introducing τ_{C} is presented further below. Equation 3 reduces to a linear viscous flow law for $n = 1$. A lin-

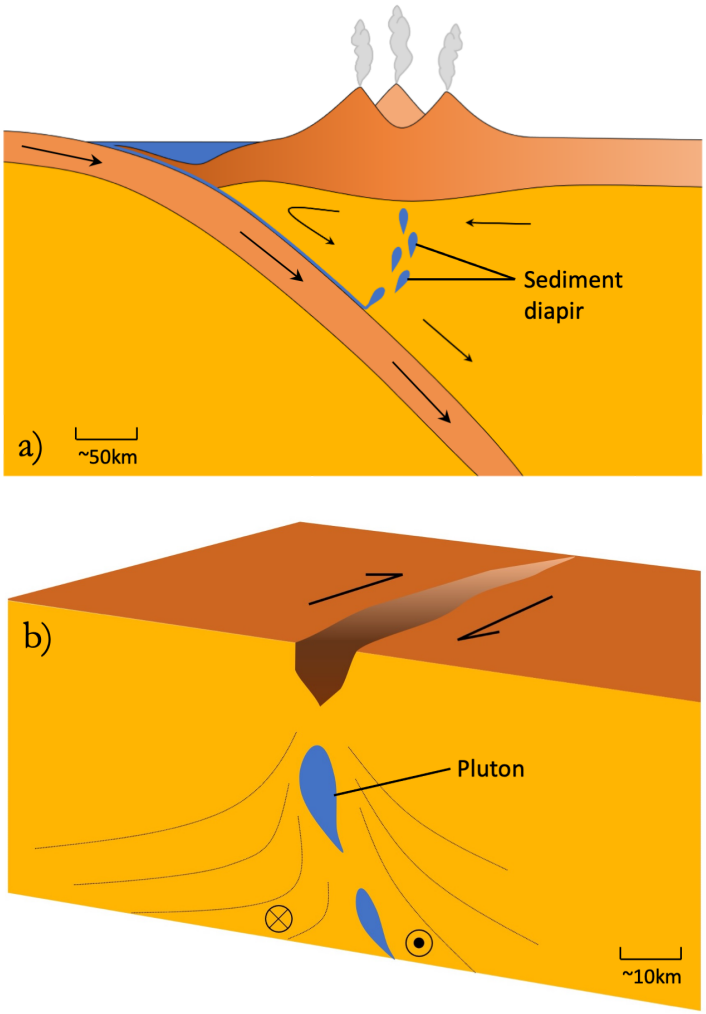

Figure 1. Sketch of two geodynamic settings in which diapirism can occur in deforming and stressed rock: a) Sediment diapirs rising in a mantle wedge (after Klein & Behn, 2021). b) Pluton rising in a crustal strike-slip zone (after Michail et al., 2021)

ear flow law typically describes diffusion creep (e.g. Karato, 2008; Turcotte & Schubert, 2021). A power-law viscous flow law typically describes dislocation creep (e.g. Karato, 2008; Turcotte & Schubert, 2021) but can also effectively describe exponential flow laws describing, for example, low temperature plasticity (e.g. Schmalholz & Fletcher, 2011). In nature, both creep mechanisms can occur simultaneously and, hence, a combination of a linear and a power-law viscous flow law is often applied in geodynamic applications (e.g. Karato, 2008). The effective viscosity, η_{E}, for such combined flow law is represented by the pseudo-harmonic mean of the linear (Equation 3 with $n = 1$) and power-law (Equation 3 with $n > 1$) viscosities and is given by (e.g. Schmalholz & Podladchikov, 2013; Gerya, 2019):

$$\eta_{\mathrm{E}} = \frac{\eta}{1 + \left(\frac{\tau}{\tau_{\mathrm{C}}}\right)^{(n-1)}} \ . \tag{4}$$

The general flow law we use in this study reads (e.g. Schmalholz & Podladchikov, 2013; Gerya, 2019):

$$\tau = 2\eta_{\mathrm{E}}\dot{\epsilon} \ . \tag{5}$$

In the combined linear and power-law viscous flow law, the magnitude of τ_{C} determines the transition from a linear viscous flow to a power-law viscous flow. Examples of magnitudes of τ_{C} for crustal and mantle flow laws, determined by rock deformation experiments, are presented in the Discussion (Section 4).

2.2 Analytical estimates for diapir ascent velocity in deforming power-law viscous medium

The ascent velocity of a diapir is controlled mostly by the effective viscosity of the surrounding medium and not by the effective viscosity of the material forming the diapir (e.g. Weinberg & Podladchikov, 1994). We assume that the effective viscosity of the surrounding medium, η_{E}, is given by Equation 4. We also assume that the effective viscosity of the diapir is smaller than the effective viscosity of the surrounding medium by a factor Ω, which is termed the viscosity ratio. For a spherical diapir with an effective viscosity that is smaller than the effective viscosity of the surrounding medium, the velocity of ascent, V, is given by (e.g. Hadamard, 1911; Rybczynski, 1911; Weinberg & Podladchikov, 1994):

$$V = \frac{1}{3}\frac{\Delta\rho g R^2}{\eta_{\mathrm{E}}} C_{\mathrm{R}} \ , \tag{6}$$

where $\Delta\rho$ is the density difference between the surrounding medium and the rising diapir, g is the gravitational acceleration, R is the radius of the sphere and the constant C_{R} is defined as (e.g. Weinberg & Podladchikov, 1994)

$$C_{\mathrm{R}} = \frac{\eta_{\mathrm{E}} + \eta_{\mathrm{E}}/\Omega}{\eta_{\mathrm{E}} + \frac{3}{2}\eta_{\mathrm{E}}/\Omega} = \frac{1 + 1/\Omega}{1 + 3/(2\Omega)} \ . \tag{7}$$

If $\tau/\tau_{\mathrm{C}} = 0$, then $\eta_{\mathrm{E}} = \eta$ (see Equation 4) and the velocity V corresponds to the ascent velocity of a linear viscous diapir rising in a linear viscous medium. We will use further below this velocity for linear viscous flow as reference velocity, V_0, to normalize the ascent velocities for power-law viscous flow. The reference velocity is

$$V_0 = \frac{1}{3}\frac{\Delta\rho g R^2}{\eta} C_{\mathrm{R}} \ . \tag{8}$$

Since for a power-law viscous flow law η_{E} depends on τ, the value of τ has to be estimated to calculate V. We consider two scenarios to estimate V: (1) There is a homogeneous regional deformation in the surrounding medium, for example a shear deformation in a strike-slip environment, which generates a regional stress τ_{R}. This value of τ_{R} is used to calculate the effective viscosity of the surrounding medium, $\eta_{\mathrm{E}}(\tau = \tau_{\mathrm{R}})$, and to calculate the rising velocity under a regional stress field, V_{R}, with Equations 6 and 7, so that

$$V_{\mathrm{R}} = V(\tau = \tau_{\mathrm{R}}) \ . \tag{9}$$

(2) Local stress variations around the diapir are caused by the diapir rising in a deformable medium. We assume that these local stress magnitudes, τ_{L}, have the same magnitude as the buoyancy stress of the diapir, $\Delta\rho g R$ (Weinberg & Podladchikov, 1994). The rising velocity for which the impact of local stress variations in the surrounding medium are considered, V_{L}, has been derived by Weinberg and Podladchikov (1994) for a power-law viscous flow law and is given by:

$$V_{\mathrm{L}} = \frac{1}{3}\frac{\Delta\rho g R^2}{\eta_{\mathrm{EL}}} C_{\mathrm{L}} \ , \tag{10}$$

where

$$C_{\mathrm{L}} = \left(\frac{G + 1/\Omega}{X_{\mathrm{sol}}(GM + 3/(2\Omega))} \right)^n \ , \tag{11}$$

with

$$\begin{aligned} G &= 2.39 - 5.15m + 3.77m^2 \\ M &= 0.76 + 0.24m \\ X_{\mathrm{sol}} &= 1.3(1 - m^2) + m \ , \end{aligned} \tag{12}$$

where $m = 1/n$. The parameter C_{L} is only a function of the two dimensionless parameters n and Ω. The effective viscosity η_{EL} for local stress variations is:

$$\eta_{\mathrm{EL}} = 2S\eta \left(\frac{6\tau_{\mathrm{C}}}{\Delta\rho g R} \right)^{(n-1)} , \tag{13}$$

where η is the viscosity parameter inside the effective viscosity (Equation 4) of the surrounding medium and S is a shape factor. The value of S will be discussed in Section 3.3. Finally, the velocity estimate for a weak diapir rising in a deforming medium with a flow law combining diffusion and dislocation creep is:

$$V_{\mathrm{D}} = V_{\mathrm{R}} + V_{\mathrm{L}} . \tag{14}$$

We normalize V_{D} by V_0 which yields

$$\frac{V_{\mathrm{D}}}{V_0} = \frac{V_{\mathrm{R}}}{V_0} + \frac{V_{\mathrm{L}}}{V_0} = 1 + \left(\frac{\tau_{\mathrm{R}}}{\tau_{\mathrm{C}}} \right)^{(n-1)} + \frac{3}{6^n S} \frac{C_{\mathrm{L}}}{C_{\mathrm{R}}} \left(\frac{\Delta\rho g R}{\tau_{\mathrm{C}}} \right)^{(n-1)} . \tag{15}$$

We will test the analytical estimate for V_{D} with 3D numerical calculations which are described below.

2.3 3D Mathematical model

We assume incompressible flow under gravity. The components of the total stress tensor, σ_{ij}, are decomposed into a pressure (mean stress), P, and deviatoric stress tensor components, τ_{ij}, so that $\sigma_{ij} = -\delta_{ij}P + \tau_{ij}$, whereby indexes i and j run from 1 to 3 and indicate the three spatial directions, and δ_{ij} is the Kronecker delta (Turcotte & Schubert, 2021). The equations for the conservation of mass for an incompressible fluid and for the conservation of linear momentum are:

$$0 = \frac{\partial V_i}{\partial x_i} \tag{16}$$

$$0 = \frac{\partial \tau_{ij}}{\partial x_j} - \frac{\partial P}{\partial x_i} + \rho g_i , \tag{17}$$

where V_i is the component of the velocity vector in direction x_i, ρ the density and g_i the gravity vector component. Components of the deviatoric stress tensor are defined as:

$$\tau_{ij} = 2\eta_{\mathrm{E}}\dot{\epsilon}_{ij} = 2\eta_{\mathrm{E}} \left(\frac{1}{2} \left(\frac{\partial V_i}{\partial x_j} + \frac{\partial V_j}{\partial x_i} \right) \right) , \tag{18}$$

where $\dot{\epsilon}_{ij}$ are the components of the deviatoric strain rate tensor and η_{E} is defined in Equation 4. For the studied 3D flow, the value of τ used in Equation 4 is quantified by the square root of the second stress invariant

$$\tau_{\mathrm{II}} = \sqrt{\tau_{xx}^2 + \tau_{yy}^2 + \tau_{zz}^2 + \tau_{xy}^2 + \tau_{xz}^2 + \tau_{yz}^2} , \tag{19}$$

which is independent of the coordinate system.

2.4 Numerical method

To numerically solve the system of governing equations (Equations 16 and 17) we discretize the differential equations using the finite difference method on a staggered grid with constant spacing (e.g. Gerya, 2019; Räss et al., 2022). We apply the pseudo-transient (PT) method to solve the discretized, non-linear equations in a matrix free fashion (e.g. Räss et al., 2022; Wang et al., 2022). The PT method is one of many iterative methods that exist since the 1950's (Frankel, 1950) and is used to solve stationary problems. The concept of the PT method is to add a pseudo-time derivative to the steady-state governing equations (e.g. Räss et al., 2022):

$$\begin{aligned} \frac{1}{\tilde{K}}\frac{\partial P}{\partial \tau_{\mathrm{PT}}} &= \frac{\partial V_i}{\partial x_i} \\ \tilde{\rho}\frac{\partial V_i}{\partial \tau_{\mathrm{PT}}} &= \frac{\partial \tau_{ij}}{\partial x_j} - \frac{\partial P}{\partial x_i} + \rho g_i \\ \frac{1}{2\tilde{G}}\frac{\partial \tau_{ij}}{\partial \tau_{\mathrm{PT}}} &= -\frac{\tau_{ij}}{2\eta_{\mathrm{E}}} + \frac{1}{2}(\nabla_i V_j + \nabla_j V_i) \ , \end{aligned} \tag{20}$$

where $\tilde{K}$, $\tilde{\rho}$ and $\tilde{G}$ are numerical parameters and τ_{PT} is a pseudo-time. $\tilde{K}$ and $\tilde{G}$ can be considered as pseudo-bulk and pseudo-shear modulus respectively, and $\tilde{\rho}$ is a pseudo-density. With the pseudo-time derivatives, Equations 20 can be considered as pseudo-acoustic and inertial approximations of the mass and momentum balance equations, respectively. The initial guess of the pressure and velocity fields do not satisfy the steady state equations, hence the PT method consists in iterating until the imbalance is sufficiently small, that is when the PT time derivatives (Equations 20) are sufficiently small and have all reached a specific tolerance value. A detailed description of the applied PT method with examples of 3D calculations is given in Räss et al. (2022). For completeness, we present a numerical resolution and tolerance test in Appendix D. For the presented results, we used a numerical resolution of $207\times207\times207$ and a tolerance for the iterative solver of $5{\cdot}10^{-7}$. The results of the resolution and tolerance test show that these values provide velocities which do not change significantly anymore for higher resolution or smaller tolerance.

We have also numerical algorithms for the studied 3D power-law viscous flow which are based on the governing equations formulated in cylindrical and spherical coordinates. These equations are given in Appendix A and Appendix B. To test our numerical implementation, we will perform numerical calculations for the same model configuration based on the governing equations in Cartesian, cylindrical and spherical coordinates. In

the limit of negligible curvature and for the same boundary and initial conditions the numerical results based on cylindrical and spherical coordinates must be identical to the results based on Cartesian coordinates. The model configuration for cylindrical and spherical coordinates is described in Appendix C.

2.5 Model configuration

The model configuration is a cube of dimension $[-L/2, L/2]\times[-L/2, L/2]\times[-L/2, L/2]$ containing a sphere of diameter $L/3$ at its center, with L indicating the model width, length and height (Figure 2). The viscosity parameter, η, of the sphere is always 100 times smaller than the one of the surrounding fluid. The applied flow law is the combined flow law given in Equation 4 and the power-law exponent is always 5. The sphere is always less dense than the surrounding fluid and we vary $\Delta\rho$ for different calculations.

We apply horizontal far-field simple shearing parallel to the horizontal x-direction (Figure 2). The boundary conditions are (i) free slip on the top and bottom faces of the cube, (ii) on the lateral sides parallel to the shearing the velocities in y- and z-direction are zero and in the x-direction they correspond to the applied far-field shearing velocity V_s ($V_x = -V_s$ for $y = -L/2$ and $V_x = V_s$ for $y = L/2$), and (iii) on the lateral sides orthogonal to the shearing the velocities in y- and z-direction are zero and the velocities in the x-direction vary linearly in the y-direction from $-V_s$ to V_s.

The model is configured in dimensionless form and also results will be displayed in dimensionless form. For the non-dimensionalization, we use three characteristic scales: one scale for length, which is the radius of the sphere R; one scale for stress, which is the buoyancy stress of the sphere $\Delta\rho g R$; and one scale for viscosity, which is the applied value of η in the surrounding medium, termed η_{m}. To describe the results, we will further use two dimensionless ratios, namely the ratio of the applied regional stress to characteristic stress, $\tau_{\mathrm{R}}/\tau_{\mathrm{C}}$, and the ratio of buoyancy stress to characteristic stress, $\Delta\rho g R/\tau_{\mathrm{C}}$. τ_{R} is the magnitude of the homogeneous shear stress in the model when the sphere has the same material properties as the surrounding material. Hence, τ_{R} represents the far-field stress which is not affected by the weak sphere.

The aims of the simulations are (i) to compare magnitudes of buoyancy stress and deviatoric stress around the sphere, (ii) to perform systematic simulations to quantify the ascent velocity of the sphere in a strike slip environment, by varying $\Delta\rho$ and τ_{C} (Equa-

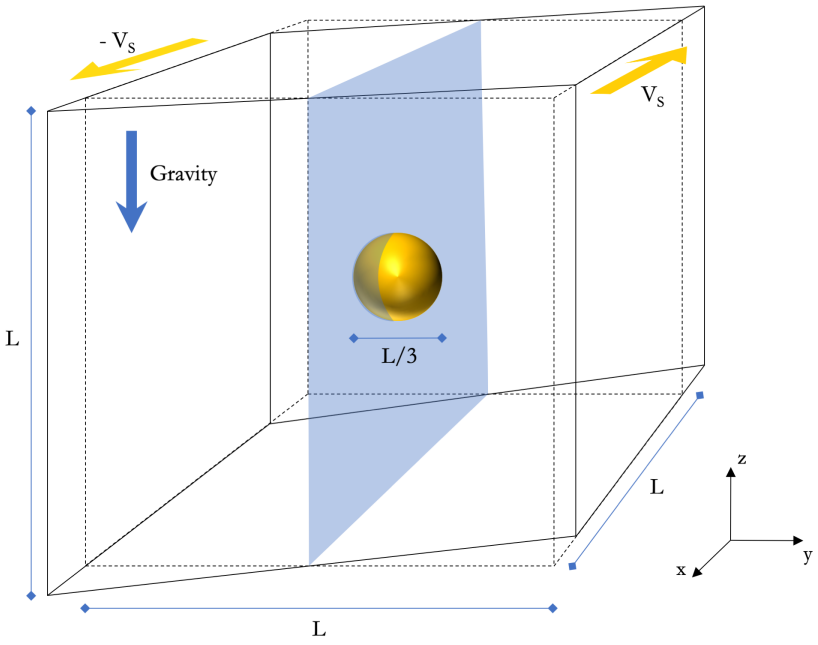

Figure 2. Model configuration: cube of size $[-L/2; L/2] \times [-L/2; L/2] \times [-L/2; L/2]$, with a less dense and weaker spherical inclusion of diameter $L/3$ at the model center. The entire model cube is sheared horizontally, parallel to the x-direction, and gravity acts in the vertical, z-direction.

tion 15), and (iii) to compare the numerically calculated velocities with the analytical estimates from Equation 15 and to improve these estimates if possible.

3 Results

3.1 Distribution of stress, pressure and effective viscosity

For each presented simulation, we have calculated one time step to obtain the full 3D velocity and stress field. First, we show the distribution of the resulting effective viscosity, η_E, the second stress invariant, τ_{II}, and the pressure, P, for a representative simulation (Figure 3). In Figure 3, 1/8th of the cubic model domain is presented. The sphere is less dense than its surrounding and, hence, moves upwards as indicated by the velocity arrows in Figure 3b. In the following, we refer to the sphere as diapir. The applied simple shear is visible on the horizontal slice through the model domain (Figure 3b). The effective viscosity shows a decrease of about one order of magnitude directly above the diapir (Figure 3b). There are two regions on the sides of the diapir where the effective

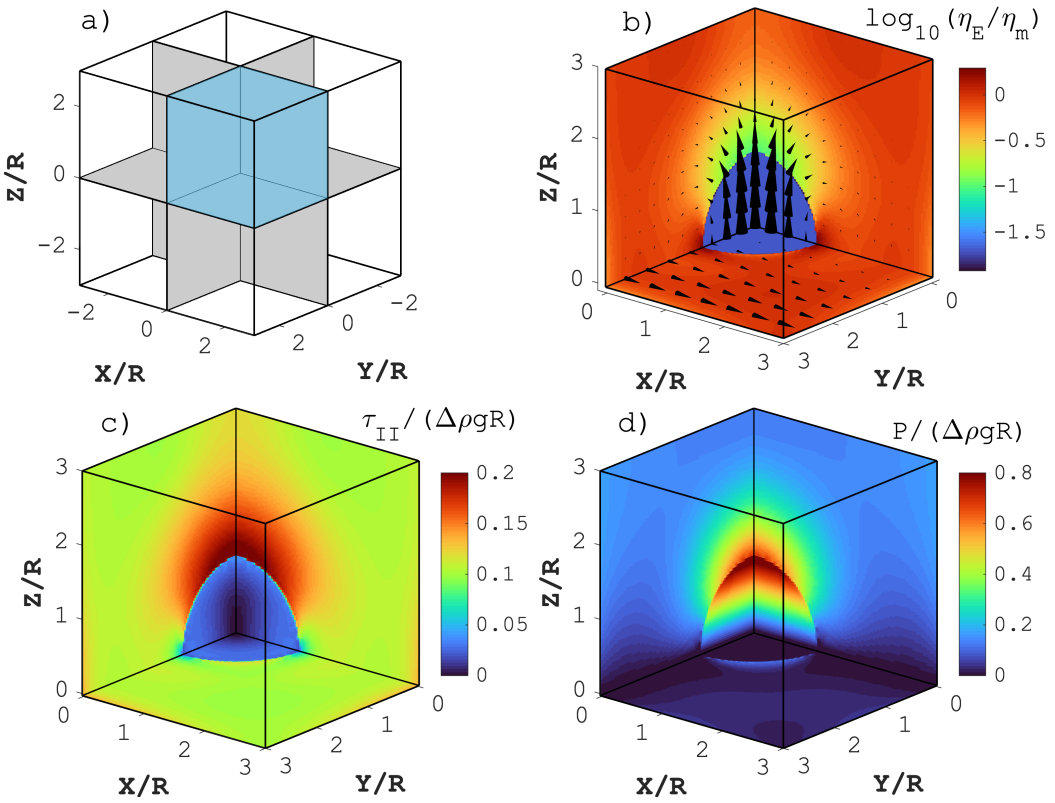

Figure 3. Representative numerical results for $\tau_R/\tau_C = 1$ and $\Delta\rho gR/\tau_C = 10$: a) Location of $1/8^{th}$ of the model shown in panels b), c) and d). b) Effective viscosity η_E normalized by η_m, the linear viscosity of the surrounding medium. Arrows indicate the velocity field. c) Second invariant of deviatoric stress, τ_{II}, normalized by the buoyancy stress $\Delta\rho gR$. d) Pressure, P, normalized by buoyancy stress $\Delta\rho gR$.

viscosity is even larger than the ambient viscosity. The variations in η_E can be explained by the distribution of τ_{II} (Figure 3c). Values of η_E are directly linked to τ_{II} (Equation 4): where the stresses are large, such as above the diapir, the effective viscosity decreases and where stresses are smaller, the effective viscosity does not change or even increases. The large stresses above the diapir are due to its upwards movement.

Figure 3d depicts the pressure field. We only consider the dynamic part of the pressure, which means that we subtract the lithostatic pressure, because only deviations from the static pressure field can cause movement. An interesting feature is the strong pressure gradient inside the diapir. Similar to the deviatoric stress, the pressure in the surrounding medium is largest directly above the diapir.

3.2 Stress decomposition and magnitudes

The total vertical stress is decomposed into the pressure and the vertical deviatoric stress, $\sigma_{\mathrm{vert}} = -P+\tau_{\mathrm{vert}}$. We quantify σ_{vert}, P and τ_{vert} and compare the magnitudes with the buoyancy stress (Figure 4). This quantification is important because the analytical estimates for the diapir velocity use the buoyancy stress as proxy for the deviatoric stress which is used in the power-law flow law.

The vertical continuity of σ_{vert} across the diapir boundary in the horizontal middle of the model (at $Y = 0$) results from the requirement of the vertical force balance. In contrast, both P and τ_{vert} can be discontinuous across the diapir boundary. Indeed, P and τ_{vert} show a discrete jump across the boundary of the diapir. The absolute maximal values of σ_{vert} are close to the value of $\Delta\rho g R$, since the maximal value of their ratio is approximately one (Figure 4a). τ_{vert} is essentially zero inside the diapir since the effective viscosity inside the diapir is 100 times smaller than the one of the surrounding medium. Consequently, the absolute magnitudes of P are high inside the diapir at the top and bottom, in order to generate a continuous σ_{vert} required by the vertical force balance. Maximal values of P inside the diapir are, hence, close to the magnitudes of $\Delta\rho g R$.

Outside the diapir, directly above and below, maximal magnitudes of τ_{vert} are significantly smaller than magnitudes of σ_{vert} at the same positions. The effective viscosity in the analytical estimate is calculated with the magnitude of $\Delta\rho g R$ while in the numerical simulation it is controlled by the correct magnitude of τ_{II}. The magnitude of τ_{II} is smaller than $\Delta\rho g R$ (Figure 3c) and τ_{II} is also strongly variable around the diapir. We, therefore, expect that the analytical estimates for the diapir velocity will be different to the numerically calculated ones, because the stress magnitude which controls the effective viscosity is different in the analytical estimates compared to the numerical simulation.

The results presented in figure 4 are reproduced by the numerical calculations based on cylindrical and spherical coordinates and are presented in Appendix C. The agreement between results calculated by three different numerical algorithms indicates the correct numerical implementation of the governing equations.

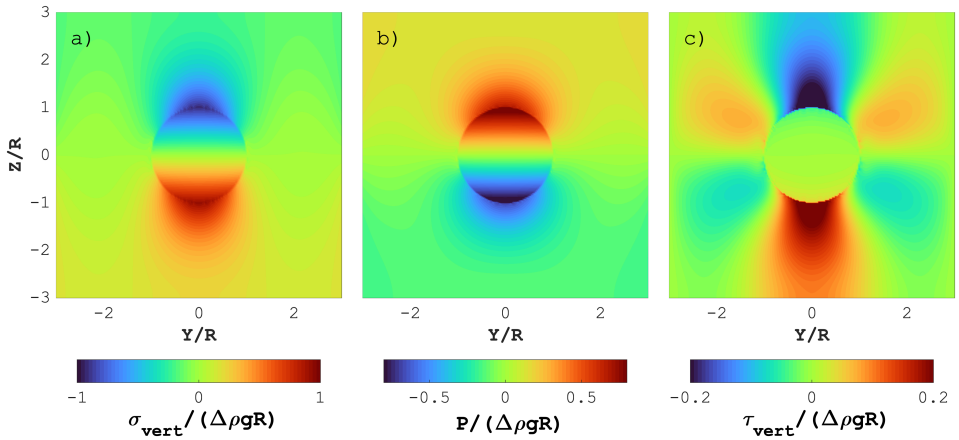

Figure 4. Numerical results for $\tau_R/\tau_C = 1$ and $\Delta\rho gR/\tau_C = 10$. Vertical cross sections at position $X/R = 0$ (see Figure 3a) of a) vertical total stress, b) pressure, and c) vertical deviatoric stress. All stresses are normalized by the buoyancy stress $\Delta\rho gR$.

3.3 Comparison of analytical and numerical ascent velocities

We compare the analytical estimates for the ascent velocity of a weak and less dense sphere, Equation 15, with our numerical results. The analytical estimates (details in Section 2.2) only provide the vertical velocity of the raising sphere and do not provide the spatial distribution of stresses. Hence, for each numerical simulation, we select the maximum vertical velocity obtained for the diapir and consider this velocity as the ascent velocity of the diapir. We normalize the vertical velocities by the corresponding values of V_0 which is the velocity of a linear viscous diapir rising in a linear viscous medium (see Equation 8).

The ascent velocity depends on the two stress ratios τ_R/τ_C and $\Delta\rho gR/\tau_C$ (Equation 15). Figure 5 presents the comparison between analytical estimates and the numerical results. Figure 5a displays vertical velocities of the diapir for various values of $\Delta\rho gR/\tau_C$ and a fixed value $\tau_R/\tau_C = 1$. For $\Delta\rho gR/\tau_C < \sim 10$ the velocity is controlled by V_R, for which the regional stress controls the effective viscosity, while for $\Delta\rho gR/\tau_C > \sim 10$ it is controlled by V_L, for which the buoyancy stress controls the effective viscosity (see Section 2.2). The velocity is constant in the domain dominated by the regional stress and increases significantly in the buoyancy dominated domain. The numerical results agree with V_R and they capture the change in slope of the velocity with increasing $\Delta\rho gR/\tau_C$. However, for $\Delta\rho gR/\tau_C > \sim 10$ the numerical velocities are smaller than the analytically

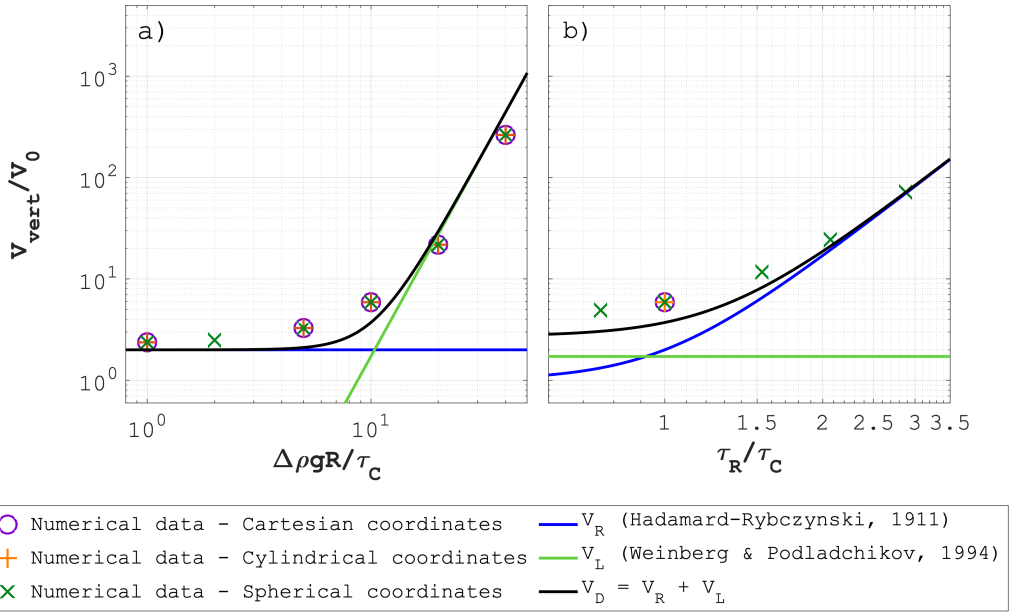

Figure 5. Comparison of numerical results (symbols, see legend) with analytical estimates from Equation 15 (lines, see legend). Analytical estimates are presented in Section 2.2. Vertical axis is the ascent velocity normalized by V_0 (see Equation 8). Horizontal axis is in a) $\Delta\rho gR/\tau_C$ for a value of $\tau_R/\tau_C = 1$, and in b) τ_R/τ_C for $\Delta\rho gR/\tau_C = 10$.

estimated ones. For $\Delta\rho gR/\tau_C > \sim 10$, the ascent velocities vary by approximately two orders of magnitude while applied values of $\Delta\rho gR/\tau_C$ vary by a factor of approximately 4 only.

Figure 5b displays the vertical velocity for various values of τ_R/τ_C and a fixed value of $\Delta\rho gR/\tau_C = 10$. The characteristic stress marks the stress at which the deformation behaviour changes from linear viscous creep to power-law viscous creep. For $\tau_R/\tau_C < \sim 1$ the velocity is controlled by V_L while for $\tau_R/\tau_C > \sim 1$ it is controlled by V_R. For $\tau_R/\tau_C > \sim 1$ the velocities strongly increase with increasing τ_R/τ_C.

We also performed a systematic comparison between the analytically estimated and the numerically calculated velocities by varying $\Delta\rho gR/\tau_C$ and τ_R/τ_C (Figure 6). Figure 6a and b display the vertical velocities of the diapir obtained with the analytical estimates and the numerical simulations, respectively. The numerical results show the same trend of the velocity with varying values of $\Delta\rho gR/\tau_C$ and τ_R/τ_C as the analytical estimates. For normalized velocities $> \sim 10^4$, the numerical algorithm did not converge any-

more due to the significant nonlinearities and the associated significant variations of the effective viscosity around the diapir.

Figure 7 is similar to Figure 5a, but shows analytical estimates for different shape factors, S (see Equation 13). The value $S = 1$ was used in the original derivation of Weinberg and Podladchikov (1994). Increasing S allows to better predict the ascent velocity in the buoyancy dominated deformation regime, that is for $\Delta\rho g R/\tau_C > 10$. However, too large values of S lead to an underestimation of the velocities. For three values of S we present the correspondence between the numerical and the analytical results. For $S = 1$, analytical estimates tend to overestimate the large velocities, for $S = 2.5$ the estimations fit better and for $S = 5$ the analytical estimates generally underestimate the ascent velocity.

A plot of all the numerically calculated velocities versus the corresponding analytical estimates, for the same parameters, shows that the analytical estimates capture well the first order trend of the numerical results (Figure 8a to c). The maximal relative error between the analytical estimate and an individual numerical result is only 72% for $S = 1$. Hence, all analytical estimates deviate by less than a factor of 2 from the numerical results. We varied S between 0.25 and 10 in the analytical estimate and calculated for each value of S the average relative error between the estimates and the numerical results (Figure 8d). The smallest average error occurs for $S = 1.6$ and is 18%.

4 Discussion

4.1 Characteristic stresses for experimentally derived flow laws

The characteristic stress, τ_C, is the stress at which the deformation behaviour changes from linear viscous flow, such as diffusion creep, to power-law viscous flow, such as dislocation creep. Hence, τ_C has a significant impact on the ascent velocity of a diapir.

To estimate values of τ_C in the mantle, we use the flow laws of olivine from Hirth and Kohlstedt (2003), their Table 1, for diffusion creep (wet olivine with constant C_{OH} and 10 mm grain size) and dislocation creep (wet olivine with constant C_{OH}) (Figure 9a). We vary systematically pressure, P, and temperature, T, and determine the stress for which the effective viscosities for diffusion and dislocation creep are equal. For P between 1 and 10 GPa and T between 500 and 1650 °C, values of τ_C are approximately between 0.1 and 100 MPa (Figure 9a).

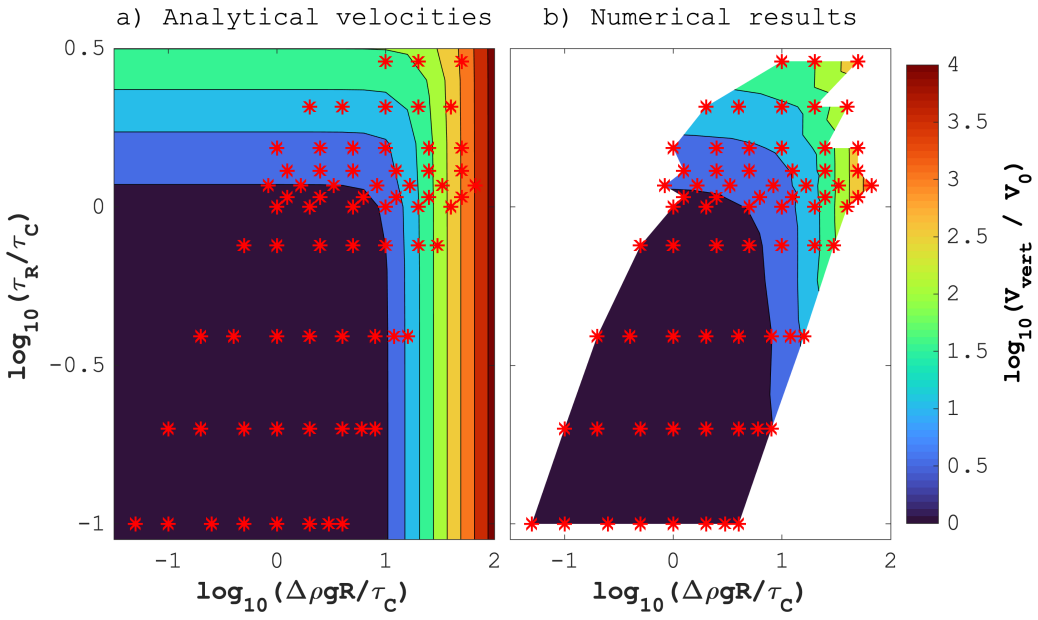

Figure 6. Analytical and numerical ascent velocities for a systematic variation of $\Delta\rho g R/\tau_{\mathrm{C}}$ and $\tau_{\mathrm{R}}/\tau_{\mathrm{C}}$. Ascent velocities are normalized by V_0 (see Equation 8). a) Analytical estimates and b) numerically calculated velocities. The stars represent the values of $\Delta\rho g R/\tau_{\mathrm{C}}$ and $\tau_{\mathrm{R}}/\tau_{\mathrm{C}}$ for which numerical calculations were performed.

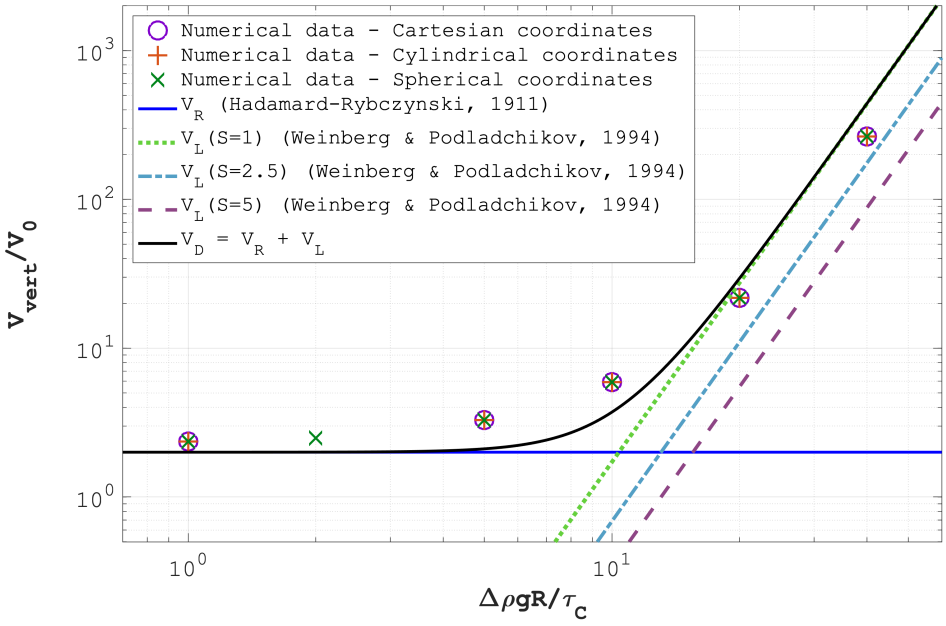

Figure 7. Comparison of numerically and analytically calculated ascent velocities for different shape factors S (see Equation 13 and legend). X-axis displays $\Delta\rho g R/\tau_{\mathrm{C}}$ and the vertical axis the ascent velocity normalized by V_0 (see Equation 8). Results are obtained for $\tau_{\mathrm{R}}/\tau_{\mathrm{C}} = 1$. Only V_{L} depends on the shape factor.

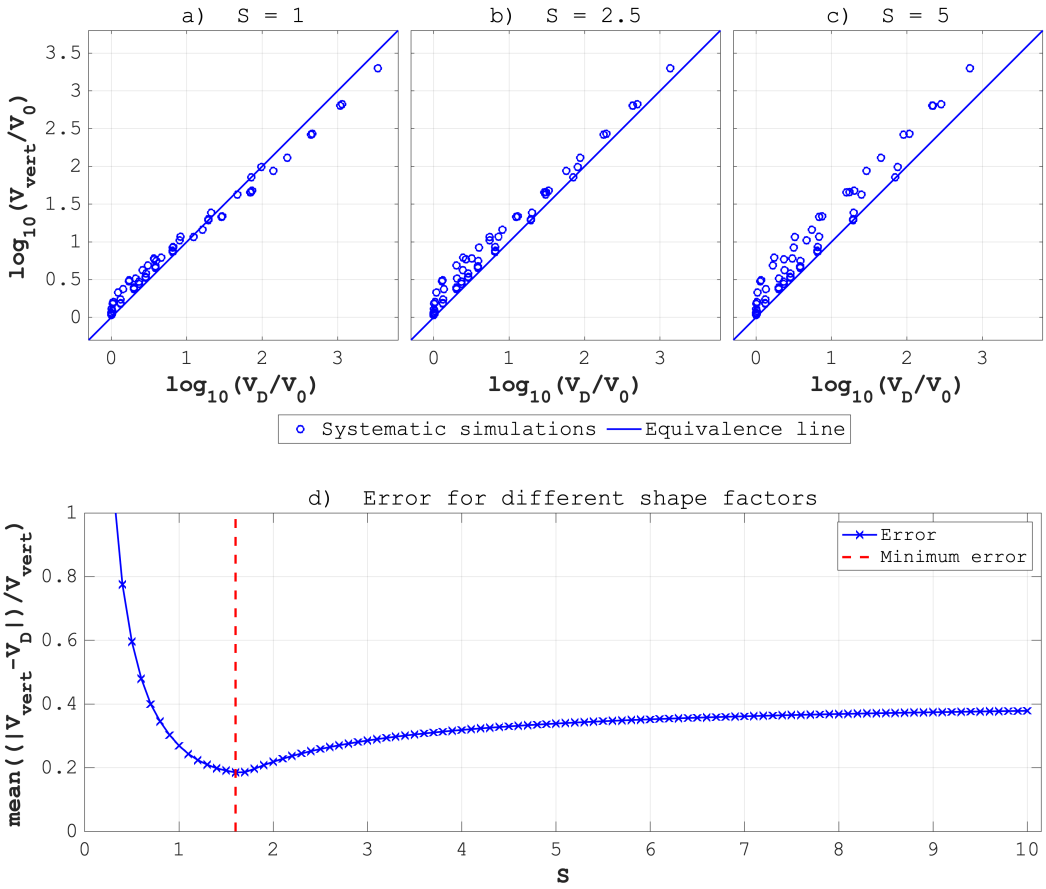

Figure 8. Comparison of analytically estimated velocities on the horizontal axis and the numerically calculated velocities on the vertical axis for different shape factors. a) $S = 1$, b) $S = 2.5$, and c) $S = 5$. The solid line represent the equivalence between analytical and numerical results. d) The average relative error of the analytical estimates compared to the numerical results for values of S between 0.25 and 10. The vertical red dashed line indicates the minimum relative error of ≈18 % for $S = 1.6$.

To estimate values of τ_C in the lower crust, we use the flow laws for diffusion and dislocation creep of wet anorthite from Rybacki and Dresen (2000), their Table 2 (Figure 9b). These flow laws are insensitive to P so we vary systematically T and the grain size to determine τ_C. For T between 500 and 1000 °C and grain size between 10 μm and 10 mm, values of τ_C are between 1 and 500 MPa.

Quartz is a representative mineral to estimate the effective flow law for upper crustal rocks. Many studies indicate that a power-law viscous flow law describes well the deformation of quartz under upper crustal conditions (e.g. Hirth et al., 2001). For extremely small grain sizes (≈20 μm), such as observed in ultramylonites, quartz can also deform by diffusion creep (Kilian et al., 2011). We did here not estimate τ_C for quartz since most studies suggest a power-law viscous flow law for quartz.

Assuming that the flow laws considered above are representative for the mantle lithosphere and the lower crust and assuming that typical regional flow stresses, representing τ_R, in the mantle are between 0.1 and 10 MPa and in the lower crust between 1 and 100 MPa, ratios of τ_R/τ_C between 0.1 and 100 seem feasible.

Furthermore, assuming that typical values of $\Delta\rho$ for diapirs vary between 20 and 200 kg/m^3 and values of R between 1 and 100 km (see next Section), provides values of $\Delta\rho g R$ between 0.2 and 200 MPa. Therefore, stress ratios of $\Delta\rho g R/\tau_C$ between 0.05 and 50 seem also feasible.

4.2 Increase of diapir ascent velocity by two types of stress weakening

In our model, the nonlinear fluid surrounding the diapir is a stress weakening fluid for $n > 1$ because the effective viscosity decreases when the stress magnitude, quantified by τ_{II}, in the fluid increases. The applied, combined linear and power-law viscous flow law can describe diffusion and dislocation creep in crustal and mantle rocks (e.g. Karato, 2008; Kohlstedt & Hansen, 2015). Furthermore, the applied power-law viscous flow law can also describe low temperature plasticity for which apparent stress exponents can be much larger than 3 (e.g. Dayem et al., 2009; Schmalholz & Fletcher, 2011). Hence, the applied combined flow law is applicable to a wide range of rocks and deformation mechanisms.

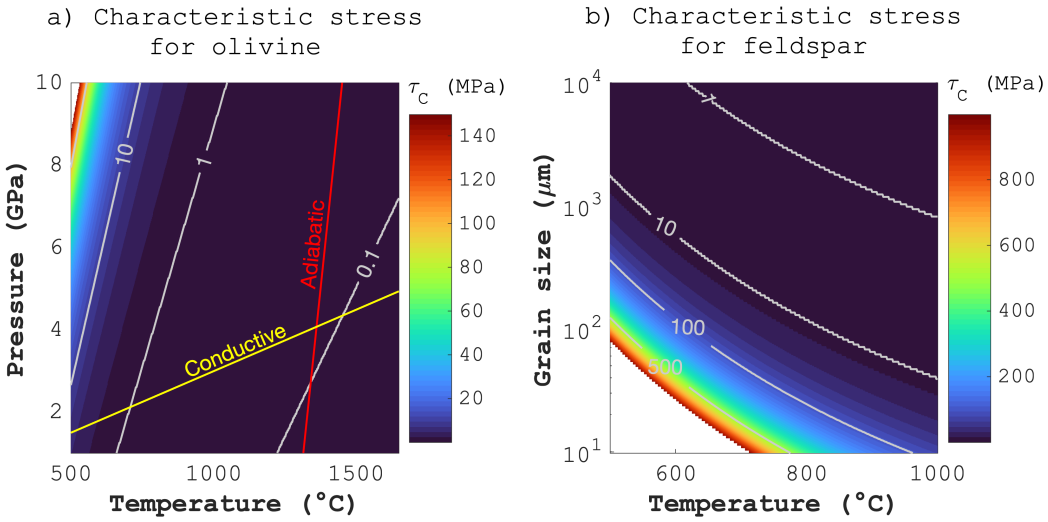

Figure 9. Color plots of characteristic stress, τ_C in Equation 4. a) τ_C as function of pressure and temperature for upper mantle flow laws. The flow laws for diffusion (wet with constant C_{OH} and $10mm$ grainsize) and dislocation (wet with constant C_{OH}) creep of olivine from Hirth and Kohlstedt (2003) (their Table 1) were used. b) τ_C as function of grain size and temperature for lower crustal flow laws. The flow laws for diffusion and dislocation creep of wet anorthite from Rybacki and Dresen (2000) (their Table 2) were used.

In the analytical estimate for the ascent velocity we consider the impact of two types of stresses: regional stresses, τ_R, associated with far-field tectonic deformation in the rocks surrounding the diapir and buoyancy stresses, $\Delta\rho gR$, causing deformation locally around the rising diapir. Both stresses can cause stress weakening. If $\tau_R/\tau_C > 1$ and/or $\Delta\rho gR/\tau_C > 1$ both stresses can increase the ascent velocity significantly (Figure 10a). For values of $n = 3$ and $\Omega = 100$, values of $\Delta\rho gR/\tau_C > \sim 10$ are required to generate values of $V_D/V_0 > 1$ and, hence, an increase in ascent velocity with respect to the velocity for linear viscous flow. The reason is the pre-factor of $3C_L/6^n/S/C_R$ in front of the term $(\Delta\rho gR/\tau_C)^{n-1}$ in the analytical velocity estimate (Equation 9). This pre-factor is 0.007 for $n = 3$ and $\Omega = 100$ and, hence, reduces the impact of the factor $\Delta\rho gR/\tau_C$ on the velocity increase (Figure 10a). Since there is no pre-factor in front of τ_R/τ_C, values of $\tau_R/\tau_C > 1$ cause values of $V_D/V_0 > 1$ (Figure 10a).

In the velocity estimate of Weinberg and Podladchikov (1994) only the impact of $\Delta\rho gR$ is considered. Hence, diapirs with small R or small $\Delta\rho$ can have values of small $\Delta\rho gR$ which might not cause a significant velocity increase. Our solution shows that also

dapirs associated with small values of $\Delta\rho g R$ can have fast ascent velocities if they rise in a tectonically active region with regional stresses $\tau_R/\tau_C > 1$. Hence, the onset of tectonic deformation, such as strike-slip shearing, transpression or transtension can trigger a faster ascent of diapirs which had insignificant ascent velocities before the onset of tectonic activity and associated stresses. Indeed, for example many plutons have been emplaced in tectonically active regions suggesting a potential causal link between pluton ascent and tectonic stress (e.g. Berdiel et al., 1997; Berger et al., 1996; Brown & Solar, 1999; Hutton & Reavy, 1992; Michail et al., 2021). We discuss the potential application of our velocity estimate to the ascent of plutons in the next Section.

For the numerical calculations, we consider a scenario with horizontal far-field simple shear. We do not model finite deformations but calculate the instantaneous velocity field. Hence, for our calculations mainly the magnitude of τ_R is important and not the orientation of the stress field. Therefore, our instantaneous solution for the far-field horizontal simple shear is approximately applicable to any scenario for which the far-field deformation causes deviatoric stresses in rocks surrounding a diapir. For example, for the ascent of diapirs within a deforming mantle wedge (e.g. Klein & Behn, 2021).

To illustrate the results with dimensional numbers, we further assume $\Delta\rho g = 2000$ Pa/m and $\tau_C = 1$ MPa (Figure 10b). For τ_R increasing above 1 MPa, the diapir velocity, V_D, increases with respect to the velocity for linear viscous flow, V_0. Concerning buoyancy stresses, values of $R > \sim 5$ km are required to obtain a velocity increase (Figure 10b). For $\tau_R = 100$ MPa the velocity would increase by four orders of magnitude and for $R \approx 15$ km the velocity would increase by one order of magnitude.

4.3 Applications to sediment diapirs, mantle plumes, (U)HP terranes and plutons

We discuss next some applications of our velocity estimate to different geodynamic settings involving diapirism. A dimensionless stress ratio which is frequently used in applications of analytical solutions to geodynamic processes is the so-called Argand number (e.g. England & McKenzie, 1982; Schmalholz et al., 2002). The Argand number is the ratio of gravity stress to stress caused by tectonic deformation (e.g. England & McKenzie, 1982; Schmalholz et al., 2002). For the considered scenario of diapirism in tectonically active regions the Argand number corresponds to the ratio $\Delta\rho g R/\tau_R$ (black con-

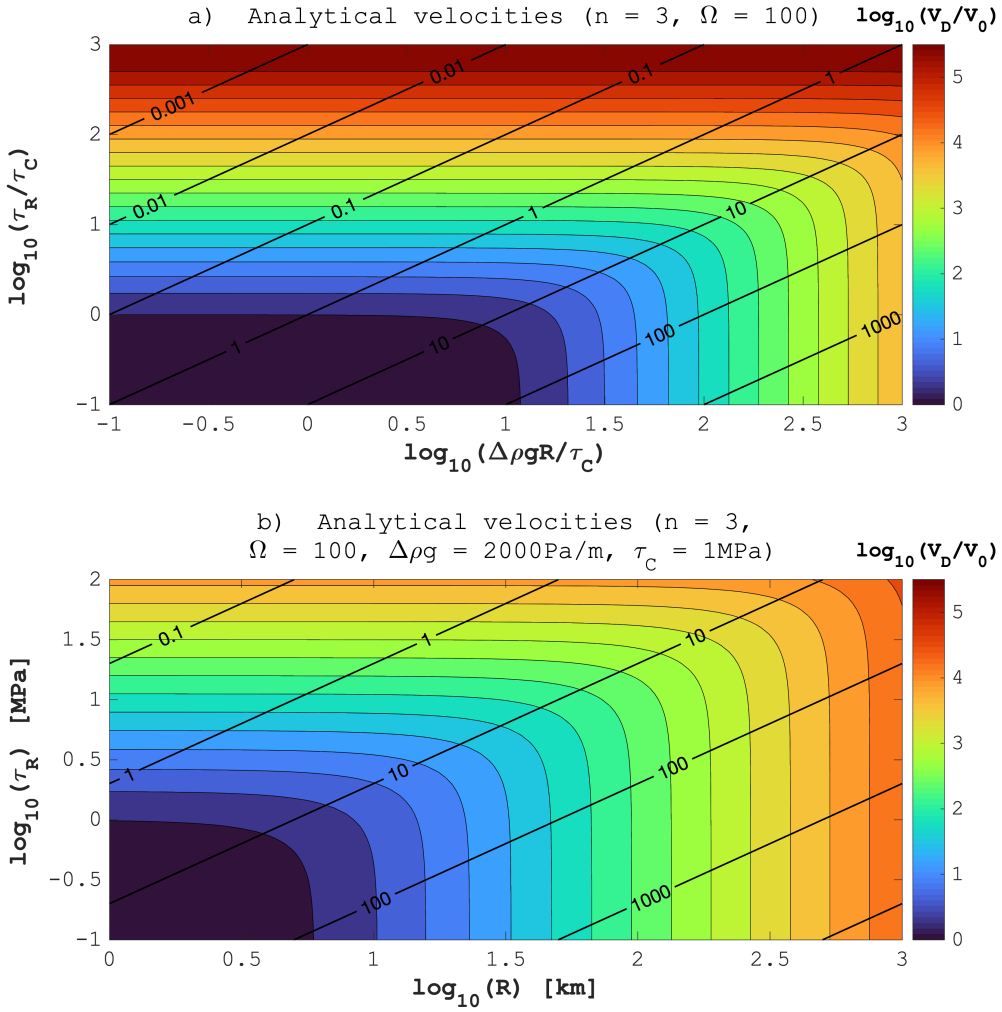

Figure 10. Color plots of analytical ascent velocities. a) Velocities (normalized by V_0) as function of $\Delta\rho g R/\tau_C$ and τ_R/τ_C for $n = 3$ and $\Omega = 100$. b) Velocities (normalized by V_0) as function of R and τ_R for $n = 3$, $\Omega = 100$, $\Delta\rho g = 2000$ Pa/m and $\tau_C = 1$ MPa. Black contour lines in both subplots indicate the corresponding values of $\Delta\rho g R/\tau_R$.

tours in Figure 10). The analytical estimate of Equation 15 can be modified so that the velocity becomes an explicit function of $\Delta\rho g R/\tau_{\mathrm{R}}$:

$$\frac{V_{\mathrm{D}}}{V_0} = 1 + \left(\frac{\tau_{\mathrm{R}}}{\tau_{\mathrm{C}}}\right)^{(n-1)} \left(1 + \frac{3}{6^n S}\frac{C_{\mathrm{L}}}{C_{\mathrm{R}}}\left(\frac{\Delta\rho g R}{\tau_{\mathrm{R}}}\right)^{(n-1)}\right) . \tag{21}$$

Values of $\Delta\rho g R/\tau_{\mathrm{R}}$ for specific geodynamic settings may be more reliably estimated than values of $\Delta\rho g R/\tau_{\mathrm{C}}$ because they do not require knowledge of the rheology.

We apply the formula for the ascent velocity, Equation 21, to sediment diapirs in subduction zones (e.g. Klein & Behn, 2021), mantle plumes (e.g. Schubert et al., 2001), exhumed (U)HP units (e.g. Burov et al., 2014) and magmatic plutons associated with crustal deformation (e.g. Michail et al., 2021) (Figure 11). For all scenarios, the values of the required parameters, such as $\Delta\rho$, R or $\tau_{\mathrm{R}}/\tau_{\mathrm{C}}$, are uncertain and we chose representative values to illustrate particular applications of Equation 21. We plot V_{D} versus R and versus the corresponding value of the Argand number for different values of the linear viscosity of the rocks surrounding the diapir, η_{m} (Figure 11). For the presented velocity calculations, we assume $\tau_{\mathrm{R}} = 10$ MPa, $n = 3$, $\tau_{\mathrm{C}} = 1$ or 10 MPa, and $\Delta\rho = 20$ or 200 kg/m^3 (Figure 11).

For sediment diapirs in subduction zones, representative values of R range between 1 and 4 km and we assume $\Delta\rho = 200$ kg/m^3 as feasible value (example 4.1.1 in Klein & Behn, 2021). Klein and Behn (2021) combined the solution of Weinberg and Podladchikov (1994) with heat transfer calculations and a melting thermodynamic model. They show that their calculated velocities for rising sediment diapirs, or relamination, can be between 10 and 100 m/yr (Figure 11a and c). To obtain such velocities, values of η_{m} must be significantly smaller than 10^{17} Pa·s, if $\tau_{\mathrm{C}} = 10$ MPa and, hence, $\tau_{\mathrm{R}}/\tau_{\mathrm{C}} = 1$ (Figure 11a). However, if $\tau_{\mathrm{C}} = 1$ MPa, values of η_{m} can be in the order of 10^{18} Pa·s to obtain the same velocities (Figure 11c). The plots in Figure 11 show that for a specific velocity a decrease of τ_{C} by one order of magnitude increases the corresponding values of η_{m} by approximately two orders of magnitude. In other words, for the same η_{m}, a decrease of τ_{C} by one order of magnitude decreases the η_{eff} by two orders of magnitude and, hence, increases the velocity by two orders of magnitude. For $n > 3$ (e.g. Klein and Behn (2021) used a flow law with $n = 3.5$), the stress weakening and velocity increase would be larger. The above example can of course be done with smaller values of τ_{R} and τ_{C}. The results suggest that to achieve the high velocities for sediment diapirs, stress weak-

ening in the surrounding rock is essential. Flow stresses in the mantle wedge, for example due to corner flow, likely contribute to the stress weakening.

For the application to mantle plumes, we assume R between 100 and 200 km and $\Delta\rho = 20$ kg/m^3 (Schubert et al., 2001) (Figure 11b and d). The ascent velocity of plumes may range between few cm/yr up to 1 m/yr (Schubert et al., 2001). To achieve such velocities, η_m needs to be between 10^{20} and 10^{21} Pa·s which agrees with viscosity estimates for the mantle (Table 11.3 in Schubert et al., 2001). Deviatoric stresses due to mantle convection may range between 0.1 and 1 MPa (e.g. Hirth & Kohlstedt, 2003) and τ_C for olivine ranges between 0.1 and 0.5 MPa for pressures between 4 and 10 GPa (Figure 9a). Therefore, values of $\tau_\mathrm{R}/\tau_\mathrm{C}$ could be >1 which would increase the corresponding ascent velocities. However, the velocities estimated for mantle plumes can be obtained without stress weakening so that for mantle plumes stress weakening seems not essential.

(U)HP crustal units, or terranes, have been exhumed in many places worldwide (e.g. Burov et al., 2014; Kylander-Clark et al., 2012). The mechanisms of exhumation are still disputed and may vary for different geodynamic settings (e.g. Hacker & Gerya, 2013; Warren, 2013). Exhumation by diapirism has been suggested as potential exhumation mechanism (e.g. Burov et al., 2001, 2014; Little et al., 2011; Schmalholz & Schenker, 2016; Schwarzenbach et al., 2021) because dapirism is able to explain the sometimes high estimates for ascent velocities of > 1 cm/yr (e.g. Hermann & Rubatto, 2014), sometimes even > 10 cm/yr (e.g. Schwarzenbach et al., 2021). Such high exhumation velocities are typically estimated for the deeper part of the exhumation path, where ambient rock pressures are $>\approx 1$ GPa. Estimates for $\Delta\rho$ for the exhumation of (U)HP units are commonly between 20 and 200 kg/m^3 and representative spherical radii, which would generate the same spherical volume as the observed (U)HP rock volume, are between 4 and 20 km (e.g. Kylander-Clark et al., 2012; Schwarzenbach et al., 2021). Stress weakening as mechanism to significantly increase ascent velocities has also been suggested as explanation for potentially fast exhumation velocities (e.g. Burov et al., 2014; Schmalholz & Schenker, 2016). For example, Schmalholz and Schenker (2016) proposed that oblique subduction and associated strike-slip shearing could have caused stress weakening along the subduction interface which might explain the high exhumation velocity, along the subduction interface, of a small UHP unit, namely the Brossasco-Isasca sub-unit in the Dora Maira massif, Western Alps.

549 The mechanisms of pluton ascent in the continental crust are still disputed and ve-
550 locities of pluton ascent are less constrained than exhumation velocities of (U)HP units.
551 Two commonly proposed mechanisms are diapirsm and dike intrusion associated with
552 fracture propagation (e.g. Clemens & Mawer, 1992; Miller & Paterson, 1999; Petford,
553 1996; Rubin, 1993). A main argument against diapirism is that estimated ascent veloc-
554 ities are so slow that the pluton would loose significant heat during ascent, consequently
555 solidify and stop ascending (e.g. Marsh, 1982; Clemens & Mawer, 1992; Petford, 1996).
556 However, Weinberg and Podladchikov (1994) suggested that stress weakening due to buoy-
557 ancy stress can increase the ascent velocity sufficiently to avoid significant heat loss dur-
558 ing ascent. Furthermore, many plutons ascended in tectonically active regions exhibit-
559 ing some component of strike-slip, transpression or transtension (e.g. Berdiel et al., 1997;
560 Berger et al., 1996; Brown & Solar, 1999; Hutton & Reavy, 1992; Michail et al., 2021).
561 The regional stresses associated with these tectonic activities could have also contributed
562 to stress weakening and velocity increase.

563 To evaluate whether stress weakening can enable a pluton to rise a significant dis-
564 tance without significant cooling, say ten times its radius, we estimate the critical ve-
565 locity, V_{C}, required for such rise, taking into account the heat loss during ascent. We per-
566 form here a very simple, back-of-the-envelope, calculation to estimate V_{C}. The time, or
567 duration, of ascent of a diapir can be calculated by $t_{\mathrm{a}} = d/V_{\mathrm{D}}$ whereby d is the distance
568 of ascent. To avoid thermal cooling during ascent, the diapir must essentially rise faster
569 than it cools. Assuming first cooling by heat conduction only, the time of cooling of a
570 diapir with radius R is $t_{\mathrm{c}} = R^2/\kappa$, whereby κ is the thermal diffusivity. Considering
571 also enhancement of cooling by advection, t_{c} can be modified by using the Nusselt num-
572 ber, Nu (e.g. Marsh, 1982), to get $t_{\mathrm{c}} = R^2/\kappa/Nu$. Solving $t_{\mathrm{c}} = t_{\mathrm{a}}$ for the velocity pro-
573 vides a critical velocity, V_{C}, for which the pluton rises as fast as it cools:

574 $$V_{\mathrm{C}} = Nu\frac{d\kappa}{R^2} \ . \tag{22}$$

575 The pluton velocity, V_{D}, must be faster than V_{C} to avoid large heat loss during ascent.
576 Assuming here that a pluton should be able to rise at least a distance of ten times its
577 radius, $d = 10R$, yields as condition for pluton ascent by diaprism:

578 $$V_{\mathrm{D}} > Nu\frac{10\kappa}{R} \ . \tag{23}$$

579 To plot also V_{C} versus R in Figure 11 we assume typical values $Nu = 2$ and $\kappa = 10^{-6}$
580 m^2/s (e.g. Marsh, 1982). We further assume R between 2 and 10 km and $\Delta\rho = 200$ $\mathrm{kg/m}^3$

as feasible values for crustal plutons (e.g. Miller & Paterson, 1999; Michail et al., 2021). Based on the above calculation, the velocity for plutons must be larger than approximately 10 cm/yr (black segment on dotted lines in Figure 11). For linear viscous flow, η_{m} of the surrounding rocks must then be smaller than approximately 10^{19} Pa·s (Figure 11a). For stress weakening due to tectonic deformation with $\tau_{\mathrm{R}}/\tau_{\mathrm{C}} = 10$, η_{m} must be smaller than approximately 10^{21} Pa·s (Figure 11c). If η_{m} is 10^{21} Pa·s and $\tau_{\mathrm{R}}/\tau_{\mathrm{C}} = 100$, then V_{D} is approximately 100 times faster than V_{C} and pluton ascent by diaprism seems possible. Our simple calculations suggest that pluton ascent by diapirism is possible if τ_{R} is high, say between 10 and 100 MPa, and τ_{C} is low, say between 0.1 and 1 MPa. More generally, tectonic activity may cause regional stresses which are significantly larger than critical stresses so that stress weakening can significantly decrease the effective viscosity of the surrounding rock. This viscosity decrease can be large enough so that plutons can rise as diapirs considerably faster than they cool.

5 Conclusions

In this study, we investigated the ascent velocity of a weak and buoyant spherical inclusion within a nonlinear viscous fluid under far-field stress, which is relevant to a wide range of natural diapirism in tectonically active regions. By deriving analytical estimates for the diapir ascent velocity in dimensionless form, we scaled the velocity with the corresponding velocity for linear viscous flow. The ascent velocity is controlled by two stress ratios: (1) the ratio of the diapir's buoyancy stress, $\Delta\rho g R$, to the characteristic stress, τ_{C}, at the transition from linear to power-law viscous flow, and (2) the ratio of regional stress, τ_{R}, to τ_{C}, whereby τ_{R} is caused by the far-field tectonic deformation. The equation for the analytical estimates shows that both stress ratios can significantly increase the velocity because the stress ratios are added and both ratios exhibit the same power-law stress exponent of $(n-1)$. The stress ratios start to considerably increase the ascent velocity once they become larger than one. Hence, both local buoyancy and regional tectonic stresses can increase the ascent velocity because they can cause stress weakening in the rocks surrounding the diapir.

Comparing the analytical estimates with full 3D numerical calculations, we found that the analytical estimates are accurate within a factor of less than two, with a relative error smaller than 80%, across a wide range of stress ratios. This highlights the usefulness of the analytical estimates in assessing the importance and impact of diapirism

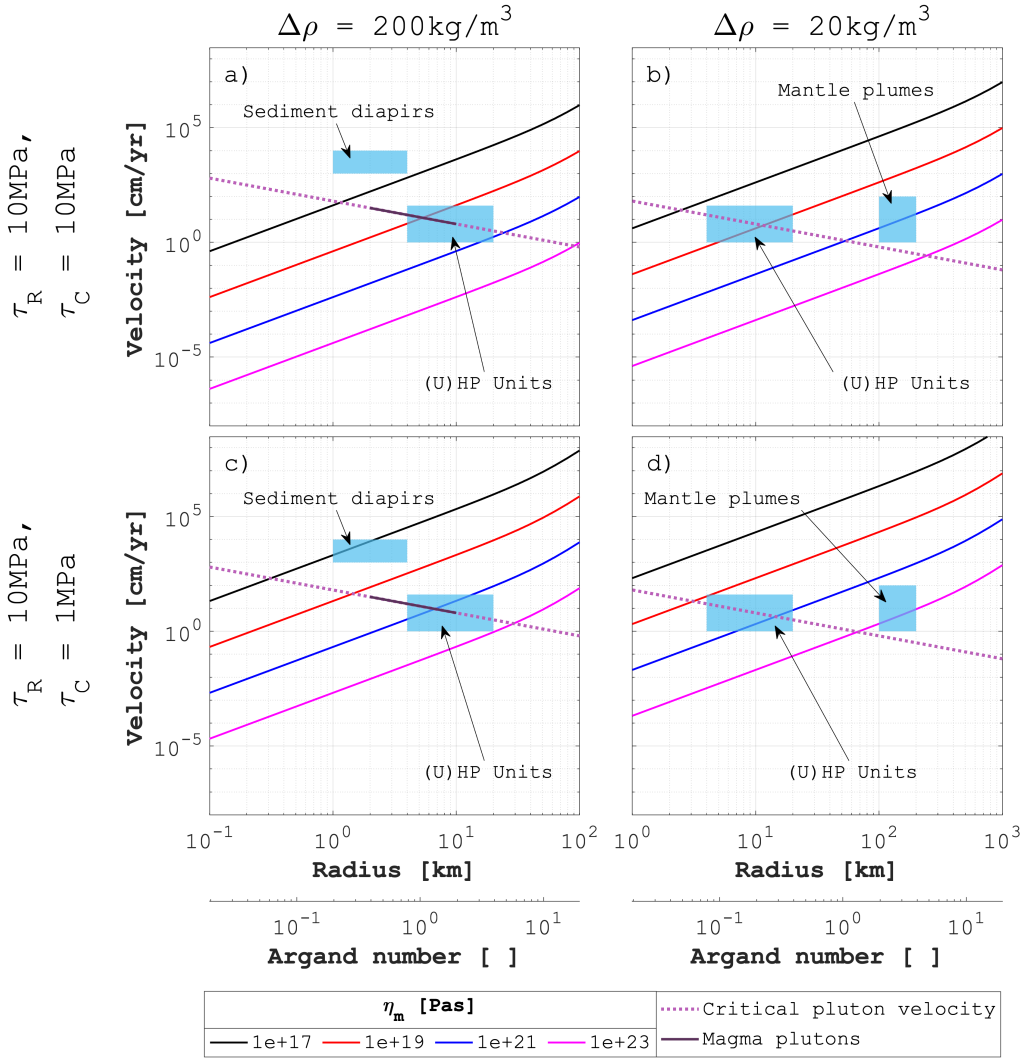

Figure 11. Analytical ascent velocities versus diapir radius and corresponding Argand number ($\Delta\rho g R/\tau_{\mathrm{R}}$) for different values of the linear viscosity, η_{m}, of the fluid surrounding the diapir. Applied values of τ_{R}, τ_{C} and $\Delta\rho$ are indicated in the figure. For all calculations n=3 and Ω=100 was used. Rectangles indicate range of data reported in literature for different geodynamic settings (see Section 4.3). The dotted line indicates the critical ascent velocity of plutons (Equation 22) for which the diapir rises as fast as it cools. The black line segment indicates the range of typical radii estimated for plutons (see Section 4.3).

in diverse geodynamic settings. However, the analytical estimates deviate the most from the numerical results when buoyancy stresses dominate the ascent velocity. This discrepancy arises because the analytical estimates use the diapir's buoyancy stress as a proxy for the deviatoric stress, which is required to calculate the effective, stress-dependent viscosity in the surrounding fluid. Numerical calculations demonstrate that deviatoric stresses around the diapir can be significantly smaller than buoyancy stresses, leading to less intense stress weakening in the surrounding fluid than predicted by the analytical estimates. Introducing a shape factor improves the accuracy of the analytical estimates. The numerical results further show that the pressure inside the weak diapir deviates from the lithostatic pressure and the deviation is on the order of $\Delta\rho g R$.

We calculated τ_{C} for typical mantle and lower crustal flow laws and estimated ranges of magnitudes for τ_{R} and $\Delta\rho g R$. Both ratios of $\tau_{\mathrm{R}}/\tau_{\mathrm{C}}$ and $\Delta\rho g R/\tau_{\mathrm{C}}$ could vary between 0.1 and 100 in nature. For the applied parameters, a significant increase of the ascent velocity caused by stress weakening starts for $\tau_{\mathrm{R}}/\tau_{\mathrm{C}} > 1$ and $\Delta\rho g R/\tau_{\mathrm{C}} > 10$. Our calculations show that stress weakening can cause ascent velocities of diapirs that are up to four orders of magnitude faster compared to ascent velocities calculated for linear viscous flow. Therefore, lithospheric and mantle stresses as well as temporal and spatial changes of these stresses can have a dramatic effect on diapir ascent velocities. Similarly, changes in rock rheology, due to for example fluid infiltration or grain size variation, can change magnitudes of τ_{C} and, consequently, strongly affect ascent velocities. The presented analytical estimates facilitate the quantification of such stress-induced changes in diapir ascent velocities.

6 Acknowledgements

This work was supported by SNSF grant No. 200020 197218. LR acknowledges the Swiss University Conference and the Swiss Council of Federal Institutes of Technology for supporting this research through the Platform for Advanced Scientific Computing (PASC) program and the Swiss National Supercomputing Centre (CSCS) through project ID c23. This work was supported by the University of Lausanne.

If this study would be eventually published we would make the applied numerical algorithm available on an open access server, such as Zenodo, so that our presented results can be reproduced.

Appendix A Cylindrical coordinate system

The equations for conservation of mass and linear momentum for an incompressible fluid under gravity in cylindrical coordinates are:

$$\begin{aligned}
0 &= -\left(\frac{\partial V_r}{\partial r}+\frac{1}{r}\frac{\partial V_\theta}{\partial \theta}+\frac{\partial V_z}{\partial z}+\frac{V_r}{r}\right)\\
0 &= \frac{\partial(-P+\tau_{rr})}{\partial r}+\frac{1}{r}\frac{\partial \tau_{r\theta}}{\partial \theta}+\frac{\partial \tau_{rz}}{\partial z}+\frac{(-P+\tau_{rr})}{r}-\frac{(-P+\tau_{\theta\theta})}{r}-\rho g\\
0 &= \frac{\partial \tau_{r\theta}}{\partial r}+\frac{1}{r}\frac{\partial(-P+\tau_{\theta\theta})}{\partial \theta}+\frac{\partial \tau_{\theta z}}{\partial z}+2\frac{\tau_{r\theta}}{r}\\
0 &= \frac{\partial \tau_{rz}}{\partial r}+\frac{1}{r}\frac{\partial \tau_{\theta z}}{\partial \theta}+\frac{\partial(-P+\tau_{zz})}{\partial z}+\frac{\tau_{rz}}{r}
\end{aligned} \tag{A1}$$

with V_r, V_θ and V_z being the components of the velocity vector in direction r, θ, and z respectively. τ_{ij} are the $(i,j)^{th}$ components of the deviatoric stress tensor, P is the pressure, ρ is the density and g the gravitational acceleration. Components of the deviatoric stress tensor are defined as:

$$\begin{aligned}
\tau_{rr} &= 2\eta_{\mathrm{E}}\dot{\epsilon}_{rr} = 2\eta_{\mathrm{E}}\left(\frac{\partial V_r}{\partial r}\right)\\
\tau_{\theta\theta} &= 2\eta_{\mathrm{E}}\dot{\epsilon}_{\theta\theta} = 2\eta_{\mathrm{E}}\left(\frac{1}{r}\frac{\partial V_\theta}{\partial \theta}+\frac{V_r}{r}\right)\\
\tau_{zz} &= 2\eta_{\mathrm{E}}\dot{\epsilon}_{zz} = 2\eta_{\mathrm{E}}\left(\frac{\partial V_z}{\partial z}\right)\\
\tau_{r\theta} &= 2\eta_{\mathrm{E}}\dot{\epsilon}_{r\theta} = 2\eta_{\mathrm{E}}\left(\frac{1}{2}\left(\frac{\partial V_\theta}{\partial r}+\frac{1}{r}\frac{\partial V_r}{\partial \theta}-\frac{V_\theta}{r}\right)\right)\\
\tau_{rz} &= 2\eta_{\mathrm{E}}\dot{\epsilon}_{rz} = 2\eta_{\mathrm{E}}\left(\frac{1}{2}\left(\frac{\partial V_z}{\partial r}+\frac{\partial V_r}{\partial z}\right)\right)\\
\tau_{\theta z} &= 2\eta_{\mathrm{E}}\dot{\epsilon}_{\theta z} = 2\eta_{\mathrm{E}}\left(\frac{1}{2}\left(\frac{1}{r}\frac{\partial V_z}{\partial \theta}+\frac{\partial V_\theta}{\partial z}\right)\right)
\end{aligned} \tag{A2}$$

where $\dot{\epsilon}_{ij}$ are the $(i,j)^{th}$ components of the strain rate tensor, and η_{E} is the effective viscosity used in the numerical calculations (see Section 2.3, Equation 4).

The numerical implementation used is the same as for the Cartesian coordinates (see Section 2.4):

$$\begin{aligned}
\frac{1}{\tilde{K}}\frac{\partial P}{\partial \tau_{\mathrm{PT}}} &= -\left(\frac{\partial V_r}{\partial r}+\frac{1}{r}\frac{\partial V_\theta}{\partial \theta}+\frac{\partial V_z}{\partial z}+\frac{V_r}{r}\right)\\
\tilde{\rho}\frac{\partial V_r}{\partial \tau_{\mathrm{PT}}} &= \frac{\partial(-P+\tau_{rr})}{\partial r}+\frac{1}{r}\frac{\partial \tau_{r\theta}}{\partial \theta}+\frac{\partial \tau_{rz}}{\partial z}+\frac{(-P+\tau_{rr})}{r}-\frac{(-P+\tau_{\theta\theta})}{r}-\rho g\\
\tilde{\rho}\frac{\partial V_\theta}{\partial \tau_{\mathrm{PT}}} &= \frac{\partial \tau_{r\theta}}{\partial r}+\frac{1}{r}\frac{\partial(-P+\tau_{\theta\theta})}{\partial \theta}+\frac{\partial \tau_{\theta z}}{\partial z}+2\frac{\tau_{r\theta}}{r}\\
\tilde{\rho}\frac{\partial V_z}{\partial \tau_{\mathrm{PT}}} &= \frac{\partial \tau_{rz}}{\partial r}+\frac{1}{r}\frac{\partial \tau_{\theta z}}{\partial \theta}+\frac{\partial(-P+\tau_{zz})}{\partial z}+\frac{\tau_{rz}}{r}
\end{aligned}$$

$$
\begin{aligned}
\frac{1}{2\tilde{G}}\frac{\partial \tau_{rr}}{\partial \tau_{\mathrm{PT}}}+\frac{\tau_{rr}}{2\eta_{\mathrm{E}}} &= \frac{\partial V_r}{\partial r}\\
\frac{1}{2\tilde{G}}\frac{\partial \tau_{\theta\theta}}{\partial \tau_{\mathrm{PT}}}+\frac{\tau_{\theta\theta}}{2\eta_{\mathrm{E}}} &= \frac{1}{r}\frac{\partial V_\theta}{\partial \theta}+\frac{V_r}{r}\\
\frac{1}{2\tilde{G}}\frac{\partial \tau_{zz}}{\partial \tau_{\mathrm{PT}}}+\frac{\tau_{zz}}{2\eta_{\mathrm{E}}} &= \frac{\partial V_z}{\partial z}\\
\frac{1}{2\tilde{G}}\frac{\partial \tau_{r\theta}}{\partial \tau_{\mathrm{PT}}}+\frac{\tau_{r\theta}}{2\eta_{\mathrm{E}}} &= \frac{1}{2}\left(\frac{\partial V_\theta}{\partial r}+\frac{1}{r}\frac{\partial V_r}{\partial \theta}-\frac{V_\theta}{r}\right)\\
\frac{1}{2\tilde{G}}\frac{\partial \tau_{rz}}{\partial \tau_{\mathrm{PT}}}+\frac{\tau_{rz}}{2\eta_{\mathrm{E}}} &= \frac{1}{2}\left(\frac{\partial V_z}{\partial r}+\frac{\partial V_r}{\partial z}\right)\\
\frac{1}{2\tilde{G}}\frac{\partial \tau_{\theta z}}{\partial \tau_{\mathrm{PT}}}+\frac{\tau_{\theta z}}{2\eta_{\mathrm{E}}} &= \frac{1}{2}\left(\frac{1}{r}\frac{\partial V_z}{\partial \theta}+\frac{\partial V_\theta}{\partial z}\right)
\end{aligned}
\tag{A3}
$$

where $\tilde{K}$, $\tilde{\rho}$ and $\tilde{G}$ are numerical parameters and τ_{PT} is a pseudo-time. $\tilde{K}$ and $\tilde{G}$ can be considered as pseudo-bulk and pseudo-shear modulus, respectively, and $\tilde{\rho}$ as a pseudo-density. With these parameters, Equation A3 can be considered as acoustic and inertial approximations of the mass and momentum balance equations respectively.

Appendix B Spherical coordinates system

The equations for conservation of mass and linear momentum for an incompressible fluid under gravity in spherical coordinates are:

$$
\begin{aligned}
0 &= -\left(\frac{\partial V_r}{\partial r}+\frac{1}{r}\frac{\partial V_\theta}{\partial \theta}+\frac{1}{r sin(\theta)}\frac{\partial V_\varphi}{\partial \varphi}+2\frac{V_r}{r}+\frac{V_\theta}{r}cot(\theta)\right)\\
0 &= \frac{\partial \sigma_{rr}}{\partial r}+\frac{1}{r}\frac{\partial \tau_{r\theta}}{\partial \theta}+\frac{1}{r sin(\theta)}\frac{\partial \tau_{r\varphi}}{\partial \varphi}+2\frac{\sigma_{rr}}{r}-\frac{\sigma_{\theta\theta}}{r}-\frac{\sigma_{\varphi\varphi}}{r}+\frac{\tau_{r\theta}}{r}cot(\theta)-\rho g\\
0 &= \frac{\partial \tau_{r\theta}}{\partial r}+\frac{1}{r}\frac{\partial \sigma_{\theta\theta}}{\partial \theta}+\frac{1}{r sin(\theta)}\frac{\partial \tau_{\theta\varphi}}{\partial \varphi}+3\frac{\tau_{r\theta}}{r}+\frac{\sigma_{\theta\theta}}{r}cot(\theta)-\frac{\sigma_{\varphi\varphi}}{r}cot(\theta)\\
0 &= \frac{\partial \tau_{r\varphi}}{\partial r}+\frac{1}{r}\frac{\partial \tau_{\theta\varphi}}{\partial \theta}+\frac{1}{r sin(\theta)}\frac{\partial \sigma_{\varphi\varphi}}{\partial \varphi}+3\frac{\tau_{r\varphi}}{r}+2\frac{\tau_{\theta\varphi}}{r}cot(\theta)
\end{aligned}
\tag{B1}
$$

with V_r, V_θ and V_φ being the components of the velocity vector in direction r, θ, and φ respectively. τ_{ij} are the $(i,j)^{th}$ components of the deviatoric stress tensor, P is the pressure, $\sigma_{ij}=-P+\tau_{ij}$ is the total stress, ρ is the density and g the gravitational acceleration. Components of the deviatoric stress tensor are defined as:

$$
\begin{aligned}
\tau_{rr} &= 2\eta_{\mathrm{E}}\dot{\epsilon}_{rr}=2\eta_{\mathrm{E}}\left(\frac{\partial V_r}{\partial r}\right)\\
\tau_{\theta\theta} &= 2\eta_{\mathrm{E}}\dot{\epsilon}_{\theta\theta}=2\eta_{\mathrm{E}}\left(\frac{1}{r}\frac{\partial V_\theta}{\partial \theta}+\frac{V_r}{r}\right)\\
\tau_{\varphi\varphi} &= 2\eta_{\mathrm{E}}\dot{\epsilon}_{\varphi\varphi}=2\eta_{\mathrm{E}}\left(\frac{1}{r sin(\theta)}\frac{\partial V_\varphi}{\partial \varphi}+\frac{V_r}{r}+\frac{V_\theta}{r}cot(\theta)\right)
\end{aligned}
$$

$$
\begin{aligned}
\tau_{r\theta} &= 2\eta_{\mathrm{E}}\dot{\epsilon}_{r\theta} = 2\eta_{\mathrm{E}}\left(\frac{1}{2}\left(\frac{\partial V_\theta}{\partial r} + \frac{1}{r}\frac{\partial V_r}{\partial \theta} - \frac{V_\theta}{r}\right)\right) \\
\tau_{r\varphi} &= 2\eta_{\mathrm{E}}\dot{\epsilon}_{r\varphi} = 2\eta_{\mathrm{E}}\left(\frac{1}{2}\left(\frac{\partial V_\varphi}{\partial r} + \frac{1}{rsin(\theta)}\frac{\partial V_r}{\partial \varphi} - \frac{V_\varphi}{r}\right)\right) \\
\tau_{\theta\varphi} &= 2\eta_{\mathrm{E}}\dot{\epsilon}_{\theta\varphi} = 2\eta_{\mathrm{E}}\left(\frac{1}{2}\left(\frac{1}{r}\frac{\partial V_\varphi}{\partial \theta} + \frac{1}{rsin(\theta)}\frac{\partial V_\theta}{\partial \varphi} - \frac{V_\varphi}{r}cot(\theta)\right)\right)
\end{aligned}
\tag{B2}
$$

where $\dot{\epsilon}_{ij}$ are the $(i,j)^{th}$ components of the strain rate tensor, and η_{E} is the effective viscosity used in the numerical calculations (see Section 2.3, Equation 4).

The numerical implementation used is the same as for the Cartesian coordinates (see Section 2.4):

$$
\begin{aligned}
\frac{1}{\tilde{K}}\frac{\partial P}{\partial \tau_{\mathrm{PT}}} &= -\left(\frac{\partial V_r}{\partial r} + \frac{1}{r}\frac{\partial V_\theta}{\partial \theta} + \frac{1}{rsin(\theta)}\frac{\partial V_\varphi}{\partial \varphi} + 2\frac{V_r}{r} - \frac{V_\theta}{r}cot(\theta)\right) \\
\tilde{\rho}\frac{\partial V_r}{\partial \tau_{\mathrm{PT}}} &= \frac{\partial \sigma_{rr}}{\partial r} + \frac{1}{r}\frac{\partial \tau_{r\theta}}{\partial \theta} + \frac{1}{rsin(\theta)}\frac{\partial \tau_{r\varphi}}{\partial \varphi} + 2\frac{\sigma_{rr}}{r} - \frac{\sigma_{\theta\theta}}{r} - \frac{\sigma_{\varphi\varphi}}{r} + \frac{\tau_{r\theta}}{r}cot(\theta) - \rho g \\
\tilde{\rho}\frac{\partial V_\theta}{\partial \tau_{\mathrm{PT}}} &= \frac{\partial \tau_{r\theta}}{\partial r} + \frac{1}{r}\frac{\partial \sigma_{\theta\theta}}{\partial \theta} + \frac{1}{rsin(\theta)}\frac{\partial \tau_{\theta\varphi}}{\partial \varphi} + 3\frac{\tau_{r\theta}}{r} + \frac{\sigma_{\theta\theta}}{r}cot(\theta) - \frac{\sigma_{\varphi\varphi}}{r}cot(\theta) \\
\tilde{\rho}\frac{\partial V_\varphi}{\partial \tau_{\mathrm{PT}}} &= \frac{\partial \tau_{r\varphi}}{\partial r} + \frac{1}{r}\frac{\partial \tau_{\theta\varphi}}{\partial \theta} + \frac{1}{rsin(\theta)}\frac{\partial \sigma_{\varphi\varphi}}{\partial \varphi} + 3\frac{\tau_{r\varphi}}{r} + 2\frac{\tau_{\theta\varphi}}{r}cot(\theta) \\
\frac{1}{2\tilde{G}}\frac{\partial \tau_{rr}}{\partial \tau_{\mathrm{PT}}} + \frac{\tau_{rr}}{2\eta_{\mathrm{E}}} &= \frac{\partial V_r}{\partial r} \\
\frac{1}{2\tilde{G}}\frac{\partial \tau_{\theta\theta}}{\partial \tau_{\mathrm{PT}}} + \frac{\tau_{\theta\theta}}{2\eta_{\mathrm{E}}} &= \frac{1}{r}\frac{\partial V_\theta}{\partial \theta} + \frac{V_r}{r} \\
\frac{1}{2\tilde{G}}\frac{\partial \tau_{\varphi\varphi}}{\partial \tau_{\mathrm{PT}}} + \frac{\tau_{\varphi\varphi}}{2\eta_{\mathrm{E}}} &= \frac{1}{rsin(\theta)}\frac{\partial V_\varphi}{\partial \varphi} + \frac{V_r}{r} + \frac{V_\theta}{r}cot(\theta) \\
\frac{1}{2\tilde{G}}\frac{\partial \tau_{r\theta}}{\partial \tau_{\mathrm{PT}}} + \frac{\tau_{r\theta}}{2\eta_{\mathrm{E}}} &= \frac{1}{2}\left(\frac{\partial V_\theta}{\partial r} + \frac{1}{r}\frac{\partial V_r}{\partial \theta} - \frac{V_\theta}{r}\right) \\
\frac{1}{2\tilde{G}}\frac{\partial \tau_{r\varphi}}{\partial \tau_{\mathrm{PT}}} + \frac{\tau_{r\varphi}}{2\eta_{\mathrm{E}}} &= \frac{1}{2}\left(\frac{\partial V_\varphi}{\partial r} + \frac{1}{rsin(\theta)}\frac{\partial V_r}{\partial \varphi} - \frac{V_\varphi}{r}\right) \\
\frac{1}{2\tilde{G}}\frac{\partial \tau_{\theta\varphi}}{\partial \tau_{\mathrm{PT}}} + \frac{\tau_{\theta\varphi}}{2\eta_{\mathrm{E}}} &= \frac{1}{2}\left(\frac{1}{r}\frac{\partial V_\varphi}{\partial \theta} + \frac{1}{rsin(\theta)}\frac{\partial V_\theta}{\partial \varphi} - \frac{V_\varphi}{r}cot(\theta)\right)
\end{aligned}
\tag{B3}
$$

where $\tilde{K}$, $\tilde{\rho}$ and $\tilde{G}$ are numerical parameters, τ_{PT} is a pseudo-time. $\tilde{K}$ and $\tilde{G}$ can be considered as pseudo-bulk and pseudo-shear modulus respectively, and $\tilde{\rho}$ as a pseudo-density. With these parameters, Equation B3 can be considered as acoustic and inertial approximations of the mass and momentum balance equations respectively.

Appendix C Comparison of Cartesian, cylindrical and spherical coordinate systems

C1 Model configuration

The model configuration in Cartesian coordinates is displayed in Figure 2. In cylindrical coordinates, the r-axis is the radial component, the θ-axis is the angular coordinate ($\theta \in [0, 2\pi]$) and the z-axis is the height of the cylinder (Figure C1a). Gravity acts in the radial direction pointing towards the central axis of the cylinder and shearing occurs along direction Z, parallel to the cylinder axis. The model configuration is essentially the same as in Cartesian coordinates (Figure 2), and a pseudo-cube, representing the model domain, is taken at the rim of the cylinder (Figure C1a). This method allows to decrease the curvature of the model domain by increasing the radius of the cylinder. In spherical coordinates, r is the radial distance, $\theta \in [0, \pi]$ is the polar angle and $\varphi \in [0, 2\pi]$ is the azimuthal angle (Figure C1b). In the spherical model, gravity acts along the radial axis, pointing towards the center of the sphere. Shearing occurs along the azimuthal axis φ. The model configuration is again essentially the same as in Cartesian coordinates (Figure 2), and a pseudo-cube is taken at the surface of the sphere. As in cylindrical coordinates, this method allows to decrease the curvature of the model domain by increasing the radius of the sphere.

As a first step of comparison of the results of the three different coordinate systems, we consider a large radius defining the curvature in the cylindrical and spherical coordinate systems. Hence, the geometry of the employed model domain for the cylindrical and spherical coordinates is essentially the same cube as for the Cartesian coordinate system. Consequently, also the applied boundary conditions are essentially identical for the three coordinates systems. The aim of these simulations is to compare the results obtained for Cartesian, cylindrical and spherical coordinates, which represents a test of three different numerical algorithms employing different system of equations. If the results from the three algorithms are equal, then the numerical implementation of the employed system of equations is correct.

C2 Results

We performed the stress quantification with three different numerical algorithms for different governing equations that are formulated for Cartesian, cylindrical and spher-

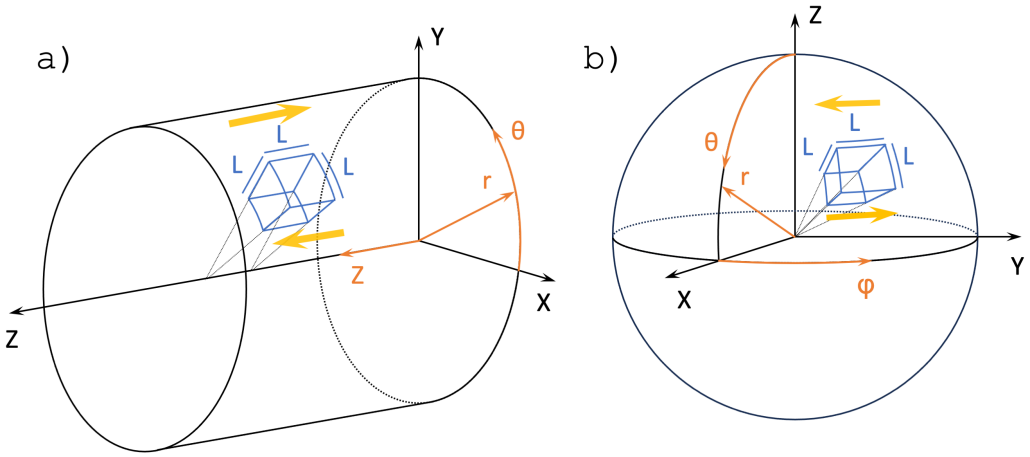

Figure C1. Model domain in a) cylindrical and, b) spherical coordinates systems. a) Cylinder is rotated so the Z-axis becomes a horizontal coordinate and gravity acts in the radial direction. The cylindrical coordinates (r, θ, Z) are displayed in orange. Model domain of size $L \times L \times L$ is taken at the rim of the cylinder (blue area) and shearing occurs in direction Z (yellow arrows). b) For the spherical coordinates, axis (r, θ, φ) are displayed in orange and gravity points towards the center of the sphere. The model domain of size $L \times L \times L$ is at the surface of the sphere (blue area) and the shearing occurs along the φ-direction (yellow arrows). In both coordinates systems, the diapir is of size $L/3$ and is located at the center of the domain (see Figure 2).

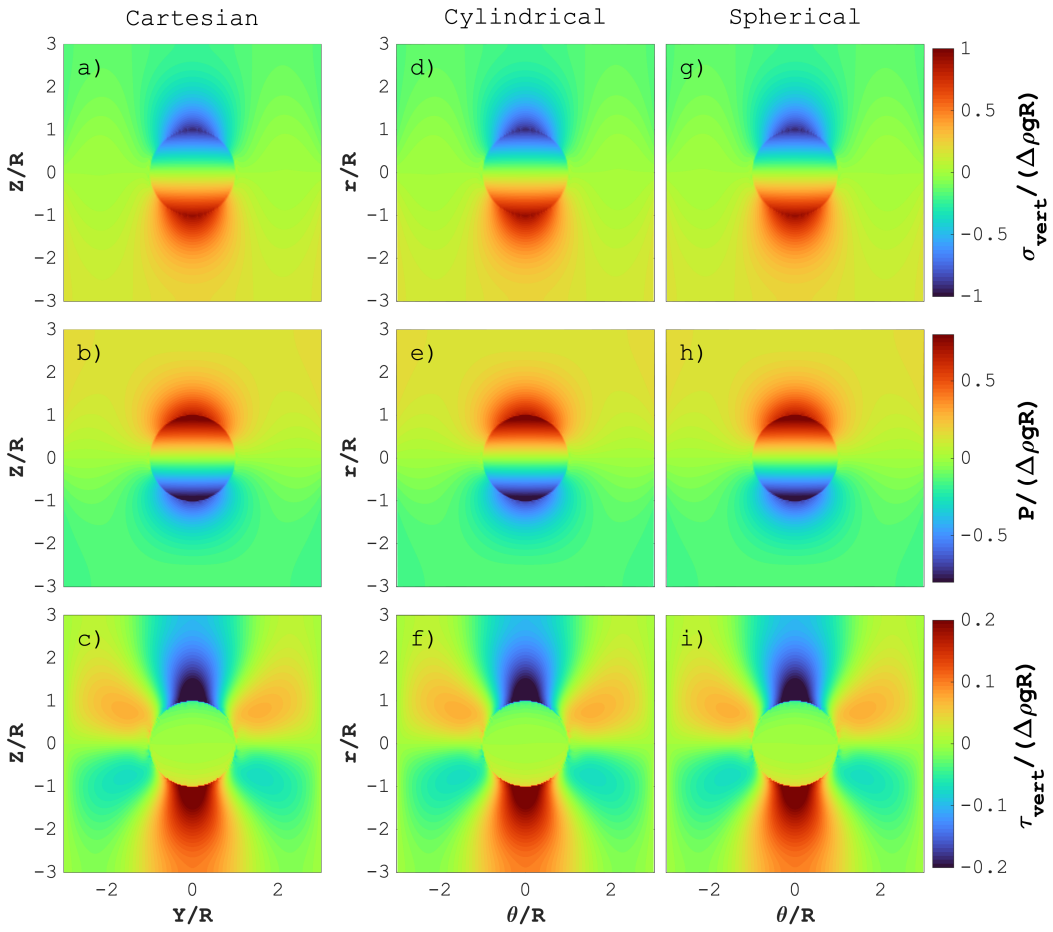

Figure C2. Numerical results for $\tau_R/\tau_C = 1$ and $\Delta\rho gR/\tau_C = 10$. Vertical cross sections at position $X/R = 0$ and $\theta/R = 0$ (see Figure 3a) of vertical total stress (a, d, g), pressure (b, e, h) and vertical deviatoric stress (c, f, i) in Cartesian (a, b, c), cylindrical (d, e, f) and spherical (g, h, i) coordinates. All stresses are normalized by the buoyancy stress $\Delta\rho gR$. For comparison, the curvature used in the cylindrical and spherical coordinates is so small that it is not visible.

ical coordinates (compare Section 2.3, Appendix A and Appendix B). Figure C2 displays the comparison between the three algorithms for the total vertical stress, pressure and vertical deviatoric stress (for a detailed explanation of these stresses and their relationship, see Section 3.2). The numerical results of the three algorithms are identical. This agreement suggests that the three algorithms and the three systems of equations are correct (Figure C2). This agreement is further confirmed by Figure 5, which shows that the maximum vertical velocities calculated by the three algorithms are equal.

Appendix D Numerical performances

Evaluating the performance of an algorithm is a challenging task, especially if one seeks at employing some absolute instead of relative metrics. In the present study, we are relying on iterative and matrix-free stencil-based solvers. In that particular configuration, we identify three criteria to evaluate performance, namely: (1) the effective memory throughput, (2) the scalability of iteration count with resolution, and (3) the parallel efficiency.

First, the effective memory throughput (Figure D1a) is used to evaluate the amount of non-redundant memory transfer that leads to saturating the memory bandwidth, which is the limiting factor in our configuration since we are memory-bound (further details in Räss et al., 2022). This means that in our implementation, data transfers between computer units and main GPU memory are the bottleneck, and not the arithmetic operations themselves. The effective memory throughput is defined as $T_{\text{eff}} = A_{\text{eff}}/t_{\text{it}}$, where A_{eff} is the effective memory access in GB and t_{it} is the time per iteration in seconds. Evaluating T_{eff} as function of resolution, we reach a plateau for resolutions larger 255 (Figure D1a). This means that passed this resolution the memory bandwidth is saturated, hence the maximal performance is reached. Also, the peak value of T_{eff}, here about 200GB/s for an Nvidia A100 GPU, means that we are about 6x below memory copy only rates (if not doing any actual computations). Further optimisations such as using shared memory to reduce cache misses could lead to bridge most of this gap, especially for 3D computations.

Second, we assess the scalability of the iteration count as function of numerical resolution (Figure D1b). The iteration count per time step normalised by the numerical grid resolution in one of the spatial direction, iter$/n_r$, remains constant and even slightly drops while resolution increases, confirming the (super-)linear scaling of the accelerated pseudo-transient method.

Third, we evaluate the parallel efficiency of our multi-GPU implementation (Figure D1c). Multi-GPU configuration is required if the problem we solve is larger than the optimal problem size we can fit onto a single GPU. In this case, we use a weak scaling approach to increase the computational resources proportionally to the global problem size. In this configuration, the parallel efficiency of the solver is important as no time should be lost in communication overhead given the distributed memory setup. Our re-

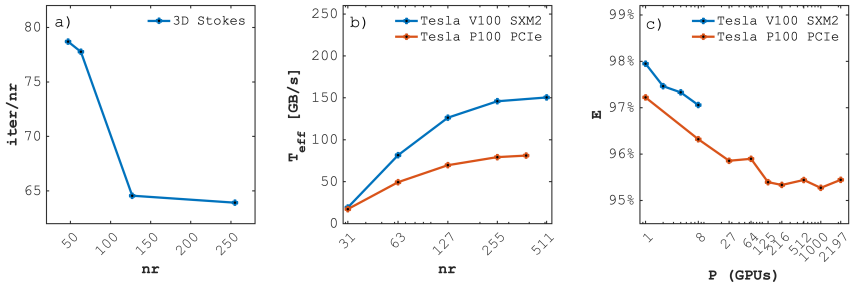

Figure D1. Performance evaluation. a) Scaling of the normalised iteration count as function of the spatial resolution n_r, b) effective memory throughput T_{eff} as function of numerical grid resolution n_r evaluated on two different GPUs (Nvidia Tesla P100 and Tesla V100), and c) the parallel efficiency E evaluated on two different GPUs.

sults show that increasing the number of GPUs has almost no effect on the time per iteration. We achieve this ideal scaling by overlapping MPI communication behind the physics calculations. Our algorithm scales ideally up to 2197 GPUs, on the Piz Daint supercomputer at the Swiss National Supercomputing Centre (CSCS). Hence it can be used to solve larger problems.

Finally, we also evaluate the sensitivity of the physical results on the numerical resolution and exit criteria (tolerance) for our iterative solver. The exit criteria represents the nonlinear tolerance value we converge the residuals to using the pseudo-transient scheme (Equation 20). Figure D2 shows that a spatial resolution of minimum 207 grid points in one of the spatial directions (total resolution is 207^3) and an exit criteria of maximum 10^{-6} are necessary to deliver accurate results.

References

Behn, M. D., Kelemen, P. B., Hirth, G., Hacker, B. R., & Massonne, H.-J. (2011). Diapirs as the source of the sediment signature in arc lavas. *Nature Geoscience*, *4*(9), 641–646.

Berdiel, T. R., Gapais, D., & Brun, J.-P. (1997). Granite intrusion along strike-slip zones in experiment and nature. *American Journal of Science*, *297*(6), 651–678.

Berger, A., Rosenberg, C., & Schmid, S. (1996). Ascent, emplacement and exhumation of the bergell pluton within the southern steep belt of the central alps.

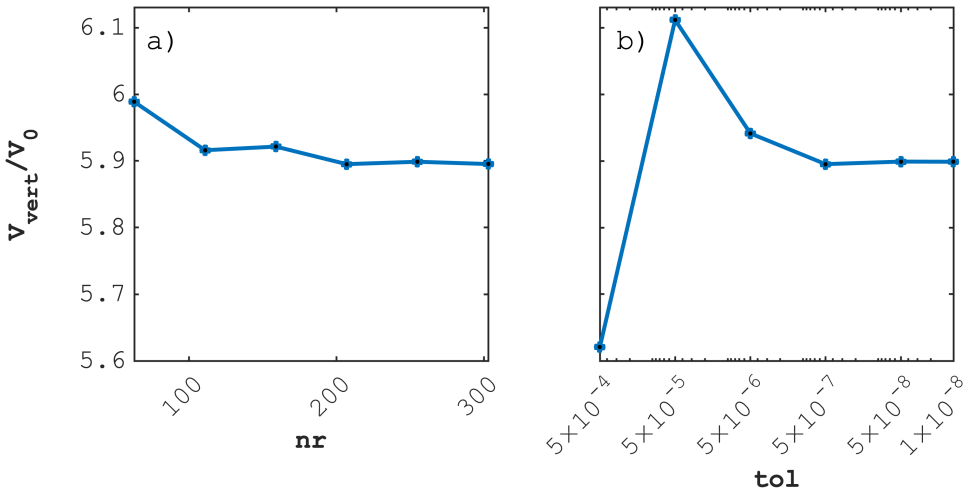

Figure D2. Numerical convergence test. a) Numerical resolution, and b) nonlinear tolerance required to obtain accurate results. Convergence is achieved when values of V_{vert}/V_0 reach a constant value.

Schweizerische mineralogische und petrographische Mitteilungen, *76*, 357–382.

Brown, M., & Solar, G. (1999). The mechanism of ascent and emplacement of granite magma during transpression: a syntectonic granite paradigm. *Tectonophysics*, *312*(1), 1–33.

Burov, E., François, T., Agard, P., Le Pourhiet, L., Meyer, B., Tirel, C., ... Brun, J.-P. (2014). Rheological and geodynamic controls on the mechanisms of subduction and hp/uhp exhumation of crustal rocks during continental collision: Insights from numerical models. *Tectonophysics*, *631*, 212–250.

Burov, E., Jaupart, C., & Guillou-Frottier, L. (2003). Ascent and emplacement of buoyant magma bodies in brittle-ductile upper crust. *Journal of Geophysical Research: Solid Earth*, *108*(B4).

Burov, E., Jolivet, L., Le Pourhiet, L., & Poliakov, A. (2001). A thermomechanical model of exhumation of high pressure (hp) and ultra-high pressure (uhp) metamorphic rocks in alpine-type collision belts. *Tectonophysics*, *342*(1-2), 113–136.

Christensen, U. (1983). Convection in a variable-viscosity fluid: Newtonian versus power-law rheology. *Earth and Planetary Science Letters*, *64*(1), 153–162.

Clemens, J., & Mawer, C. (1992). Granitic magma transport by fracture propaga-

tion. *Tectonophysics*, *204*(3-4), 339–360.

Cruden, A. R. (1988). Deformation around a rising diapir modeled by creeping flow past a sphere. *Tectonics*, *7*(5), 1091-1101. Retrieved from `https://agupubs.onlinelibrary.wiley.com/doi/abs/10.1029/TC007i005p01091` doi: https://doi.org/10.1029/TC007i005p01091

Cruden, A. R., & Weinberg, R. (2018). Mechanisms of magma transport and storage in the lower and middle crust—magma segregation, ascent and emplacement. *Volcanic and igneous plumbing systems*, 13–53.

Dayem, K. E., Houseman, G. A., & Molnar, P. (2009). Localization of shear along a lithospheric strength discontinuity: Application of a continuous deformation model to the boundary between tibet and the tarim basin. *Tectonics*, *28*(3).

England, P., & McKenzie, D. (1982). A thin viscous sheet model for continental deformation. *Geophysical Journal International*, *70*(2), 295–321.

Fletcher, R. C. (1974). Wavelength selection in the folding of a single layer with power-law rheology. *American Journal of Science*, *274*(9), 1029–1043.

Frankel, S. P. (1950). Convergence rates of iterative treatments of partial differential equations. *Math. Comput.*, *4*, 65-75.

Gerya, T. (2019). *Introduction to numerical geodynamic modelling.* CAMBRIDGE. Retrieved from `https://www.ebook.de/de/product/34700198/taras_gerya_introduction_to_numerical_geodynamic_modelling.html`

Gerya, T., & Yuen, D. A. (2003). Rayleigh–taylor instabilities from hydration and melting propel 'cold plumes' at subduction zones. *Earth and Planetary Science Letters*, *212*(1-2), 47–62.

Hacker, B. R., & Gerya, T. V. (2013). Paradigms, new and old, for ultrahigh-pressure tectonism. *Tectonophysics*, *603*, 79–88.

Hadamard, J. (1911). Mouvement permanent lent d'une sphere liquide et visqueuse dans un liquid visqueux. *C. R. Acad Sci.*, *152*, 1735-1738.

Hermann, J., & Rubatto, D. (2014). Subduction of continental crust to mantle depth: geochemistry of ultrahigh-pressure rocks. In *Treatise on geochemistry, 2nd edition.* Elsevier.

Hirth, G., & Kohlstedt, D. (2003). Rheology of the upper mantle and the mantle wedge: A view from the experimentalists. *Geophysical monograph-american geophysical union*, *138*, 83–106.

Hirth, G., Teyssier, C., & Dunlap, J. W. (2001). An evaluation of quartzite flow laws based on comparisons between experimentally and naturally deformed rocks. *International Journal of Earth Sciences*, *90*, 77–87.

Hutton, D., & Reavy, R. (1992). Strike-slip tectonics and granite petrogenesis. *Tectonics*, *11*(5), 960–967.

Jackson, M., Cornelius, R., Craig, C., Gansser, A., Stöcklin, J., & Talbot, C. (1990). Salt diapirs of the great kavir, central iran.

Jackson, M., & Vendeville, B. (1994). Regional extension as a geologic trigger for diapirism. *Geological society of America bulletin*, *106*(1), 57–73.

Karato, S.-i. (2008). Deformation of earth materials. *An introduction to the rheology of Solid Earth*, *463*.

Kilian, R., Heilbronner, R., & Stünitz, H. (2011). Quartz grain size reduction in a granitoid rock and the transition from dislocation to diffusion creep. *Journal of Structural Geology*, *33*(8), 1265–1284.

Klein, B. Z., & Behn, M. D. (2021). On the evolution and fate of sediment diapirs in subduction zones. *Geochemistry, Geophysics, Geosystems*, *22*(11), e2021GC009873. Retrieved from `https://agupubs.onlinelibrary.wiley.com/doi/abs/10.1029/2021GC009873` (e2021GC009873 2021GC009873) doi: https://doi.org/10.1029/2021GC009873

Kohlstedt, D., & Hansen, L. (2015). 2.18 - constitutive equations, rheological behavior, and viscosity of rocks. In G. Schubert (Ed.), *Treatise on geophysics (second edition)* (Second Edition ed., p. 441-472). Oxford: Elsevier. Retrieved from `https://www.sciencedirect.com/science/article/pii/B9780444538024000427` doi: https://doi.org/10.1016/B978-0-444-53802-4.00042-7

Kylander-Clark, A. R., Hacker, B. R., & Mattinson, C. G. (2012). Size and exhumation rate of ultrahigh-pressure terranes linked to orogenic stage. *Earth and Planetary Science Letters*, *321*, 115–120.

Larsen, T. B., & Yeun, D. A. (1997). Fast plumeheads: Temperature-dependent versus non-newtonian rheology. *Geophysical Research Letters*, *24*(16), 1995–1998.

Little, T., Hacker, B., Gordon, S., Baldwin, S., Fitzgerald, P., Ellis, S., & Korchinski, M. (2011). Diapiric exhumation of earth's youngest (uhp) eclogites in the gneiss domes of the d'entrecasteaux islands, papua new guinea. *Tectono-*

physics, *510*(1-2), 39–68.

Marschall, H. R., & Schumacher, J. C. (2012). Arc magmas sourced from mélange diapirs in subduction zones. *Nature Geoscience*, *5*(12), 862–867.

Marsh, B. D. (1982). On the mechanics of igneous diapirism, stoping, and zone melting. *American Journal of Science*, *282*(6), 808–855.

Mazzini, A., Nermoen, A., Krotkiewski, M., Podladchikov, Y., Planke, S., & Svensen, H. (2009). Strike-slip faulting as a trigger mechanism for overpressure release through piercement structures. implications for the lusi mud volcano, indonesia. *Marine and Petroleum Geology*, *26*(9), 1751–1765.

Michail, M., Rudolf, M., Rosenau, M., Riva, A., Gianolla, P., & Coltorti, M. (2021). Shape of plutons in crustal shear zones: A tectono-magmatic guide based on analogue models. *Journal of Structural Geology*, *150*, 104417. Retrieved from `https://www.sciencedirect.com/science/article/pii/S0191814121001413` doi: https://doi.org/10.1016/j.jsg.2021.104417

Miller, R. B., & Paterson, S. R. (1999). In defense of magmatic diapirs. *Journal of Structural Geology*, *21*(8), 1161-1173. Retrieved from `https://www.sciencedirect.com/science/article/pii/S0191814199000334` doi: https://doi.org/10.1016/S0191-8141(99)00033-4

Nahas, I., Gonçalves, L., Gonçalves, C. C., & Raposo, M. I. B. (2023). Unraveling the relationship between a tonalitic pluton and shear zones: Insights from magnetic fabrics and microstructures of the alto maranhão batholith, mineiro belt, southern são francisco craton. *Journal of Structural Geology*, 104887. Retrieved from `https://www.sciencedirect.com/science/article/pii/S0191814123001049` doi: https://doi.org/10.1016/j.jsg.2023.104887

Petford, N. (1996). Dykes or diapirs? *Earth and Environmental Science Transactions of the Royal Society of Edinburgh*, *87*(1-2), 105–114.

Plank, T., & Langmuir, C. H. (1993). Tracing trace elements from sediment input to volcanic output at subduction zones. *Nature*, *362*(6422), 739–743.

Poliakov, A. N., Podladchikov, Y., & Talbot, C. (1993). Initiation of salt diapirs with frictional overburdens: numerical experiments. *Tectonophysics*, *228*(3-4), 199–210.

Poliakov, A. N., Podladchikov, Y. Y., Dawson, E. C., & Talbot, C. J. (1996). Salt diapirism with simultaneous brittle faulting and viscous flow. *Geological Soci-*

ety, London, Special Publications, *100*(1), 291–302.

Rabinowicz, M., Ceuleneer, G., & Nicolas, A. (1987). Melt segregation and flow in mantle diapirs below spreading centers: Evidence from the oman ophiolite. *Journal of Geophysical Research: Solid Earth*, *92*(B5), 3475-3486. Retrieved from `https://agupubs.onlinelibrary.wiley.com/doi/abs/10.1029/JB092iB05p03475` doi: https://doi.org/10.1029/JB092iB05p03475

Ramberg, H. (1968). Fluid dynamics of layered systems in the field of gravity, a theoretical basis for certain global structures and isostatic adjustment. *Physics of the Earth and Planetary Interiors*, *1*(2), 63–87.

Räss, L., Utkin, I., Duretz, T., Omlin, S., & Podladchikov, Y. Y. (2022). Assessing the robustness and scalability of the accelerated pseudo-transient method. *Geoscientific Model Development*, *15*(14), 5757–5786.

Rubin, A. M. (1993). Dikes vs. diapirs in viscoelastic rock. *Earth and Planetary Science Letters*, *117*(3-4), 653–670.

Rybacki, E., & Dresen, G. (2000). Dislocation and diffusion creep of synthetic anorthite aggregates. *Journal of Geophysical Research: Solid Earth*, *105*(B11), 26017–26036.

Rybczynski, W. (1911). Über die fortschreitende bewegung einer flüssigen kugel in einen zähen medium, bull. *Acad. Sci. Cracovie*, *1*, 40-46.

Schmalholz, S. M., & Fletcher, R. C. (2011). The exponential flow law applied to necking and folding of a ductile layer. *Geophysical Journal International*, *184*(1), 83–89.

Schmalholz, S. M., Podladchikov, Y., & Burg, J.-P. (2002). Control of folding by gravity and matrix thickness: Implications for large-scale folding. *Journal of Geophysical Research: Solid Earth*, *107*(B1), ETG–1.

Schmalholz, S. M., & Podladchikov, Y. Y. (2013). Tectonic overpressure in weak crustal-scale shear zones and implications for the exhumation of high-pressure rocks. *Geophysical Research Letters*, *40*(10), 1984–1988. doi: 10.1002/grl.50417

Schmalholz, S. M., & Schenker, F. L. (2016). Exhumation of the dora maira ultrahigh-pressure unit by buoyant uprise within a low-viscosity mantle oblique-slip shear zone. *Terra Nova*, *28*(5), 348–355.

Schubert, G., Turcotte, D. L., & Olson, P. (2001). *Mantle convection in the earth*

and planets. Cambridge University Press.

Schultz-Ela, D., Jackson, M., & Vendeville, B. (1993). Mechanics of active salt diapirism. *Tectonophysics*, *228*(3), 275-312. Retrieved from https://www.sciencedirect.com/science/article/pii/004019519390345K doi: https://doi.org/10.1016/0040-1951(93)90345-K

Schwarzenbach, E. M., Zhong, X., Caddick, M. J., Schmalholz, S. M., Menneken, M., Hecht, L., & John, T. (2021). On exhumation velocities of high-pressure units based on insights from chemical zoning in garnet (tianshan, nw china). *Earth and Planetary Science Letters*, *570*, 117065.

Smye, A. J., & England, P. C. (2023). Metamorphism and deformation on subduction interfaces: 2. petrological and tectonic implications. *Geochemistry, Geophysics, Geosystems*, *24*(1), e2022GC010645.

Stokes, G. (1850). On the effect of internal friction of fluids on the motion of pendulums. *Trans. Camb. phi1. S0c*, *9*(8), 106.

Turcotte, D., & Schubert, G. (2021). *Geodynamics*. Cambridge University Press. Retrieved from https://www.ebook.de/de/product/21880842/donald_turcotte_gerald_schubert_geodynamics.html

Wang, L. H., Yarushina, V. M., Alkhimenkov, Y., & Podladchikov, Y. (2022). Physics-inspired pseudo-transient method and its application in modelling focused fluid flow with geological complexity. *Geophysical Journal International*, *229*(1), 1–20.

Warren, C. (2013). Exhumation of (ultra-) high-pressure terranes: concepts and mechanisms. *Solid Earth*, *4*(1), 75–92.

Weinberg, R. F., & Podladchikov, Y. (1994). Diapiric ascent of magmas through power law crust and mantle. *Journal of Geophysical Research: Solid Earth*, *99*(B5), 9543–9559. doi: 10.1029/93jb03461

Weinberg, R. F., & Podladchikov, Y. Y. (1995). The rise of solid-state diapirs. *Journal of Structural Geology*, *17*(8), 1183–1195.

Whitehead Jr., J. A., & Luther, D. S. (1975). Dynamics of laboratory diapir and plume models. *Journal of Geophysical Research (1896-1977)*, *80*(5), 705-717. Retrieved from https://agupubs.onlinelibrary.wiley.com/doi/abs/10.1029/JB080i005p00705 doi: https://doi.org/10.1029/JB080i005p00705

Figure 1.

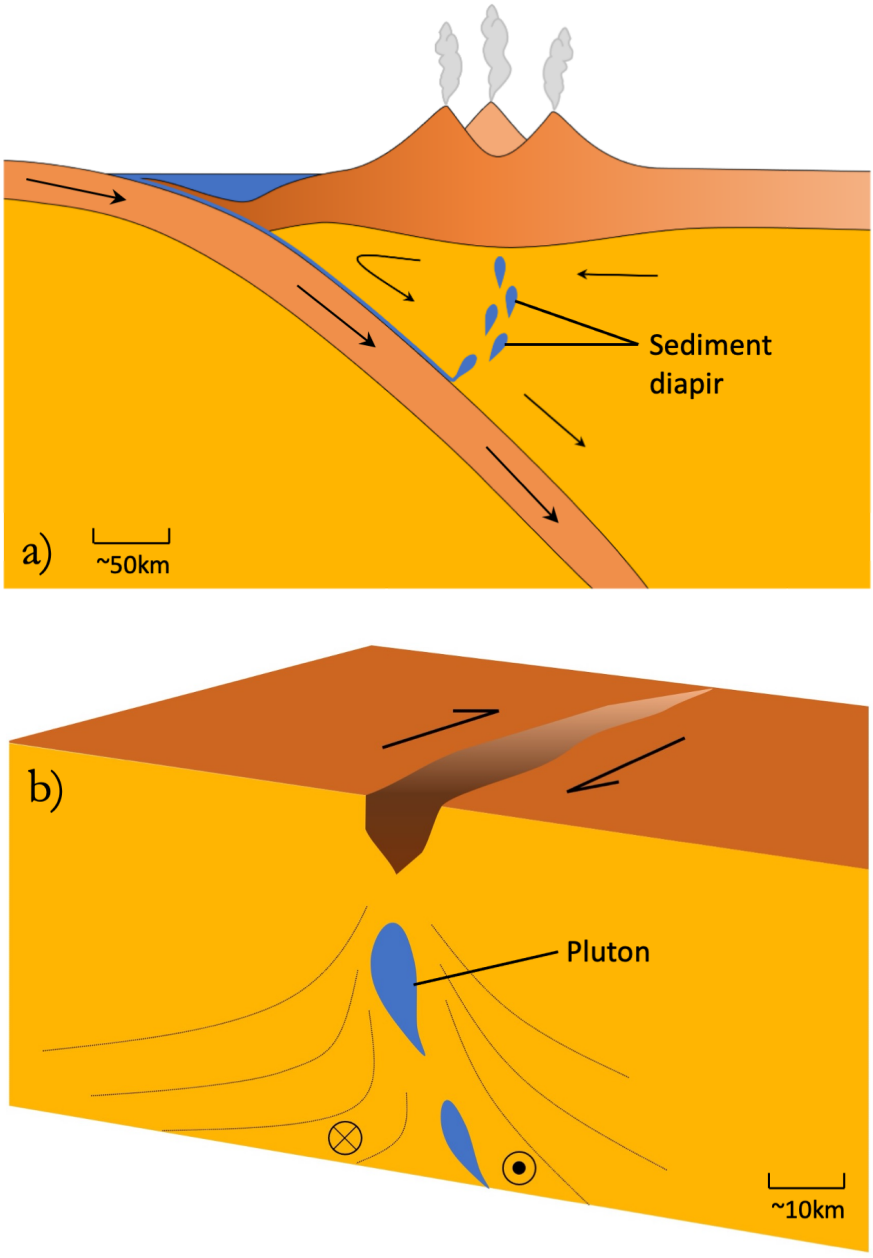
Sediment
diapir
a)
~50km
b)
Pluton
~10km

Figure 2.

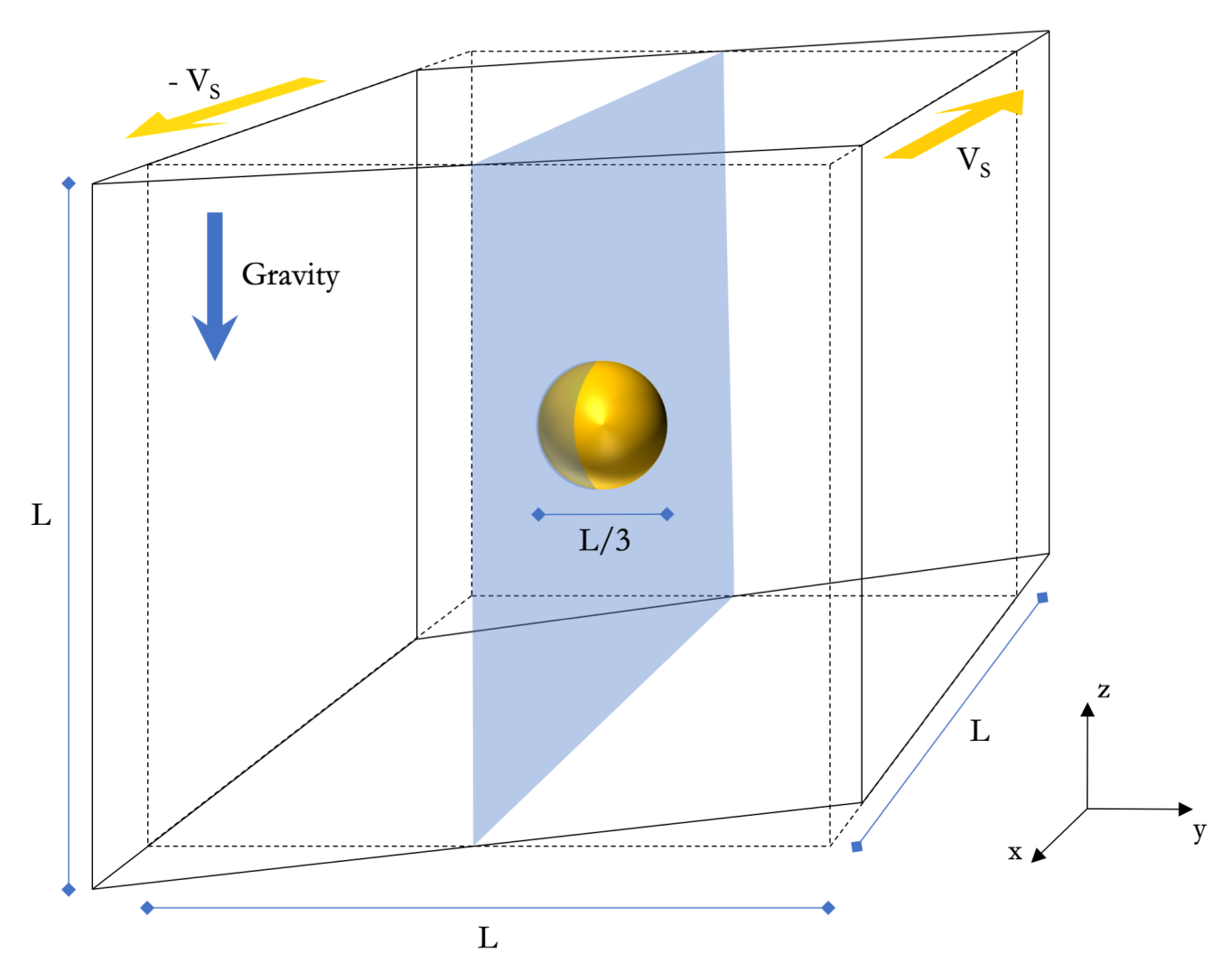
- V_S
V_S
Gravity
L
L/3
L
L
z
y
x

Figure 3.

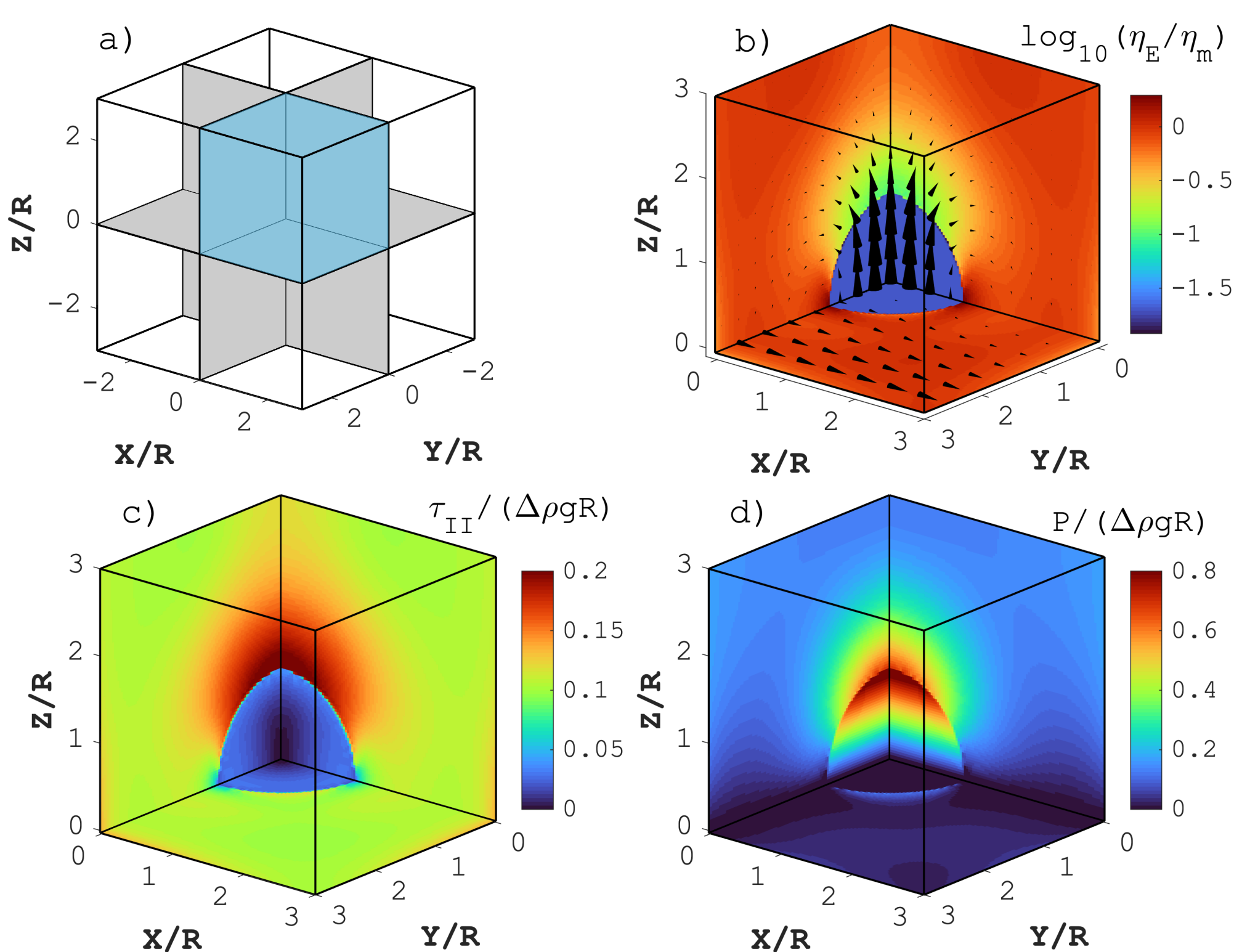
a)
Z/R
X/R
Y/R
b)
$\log_{10}(\eta_E/\eta_m)$
Z/R
X/R
Y/R
c)
$\tau_{II}/(\Delta\rho gR)$
Z/R
X/R
Y/R
d)
$P/(\Delta\rho gR)$
Z/R
X/R
Y/R

Figure 4.

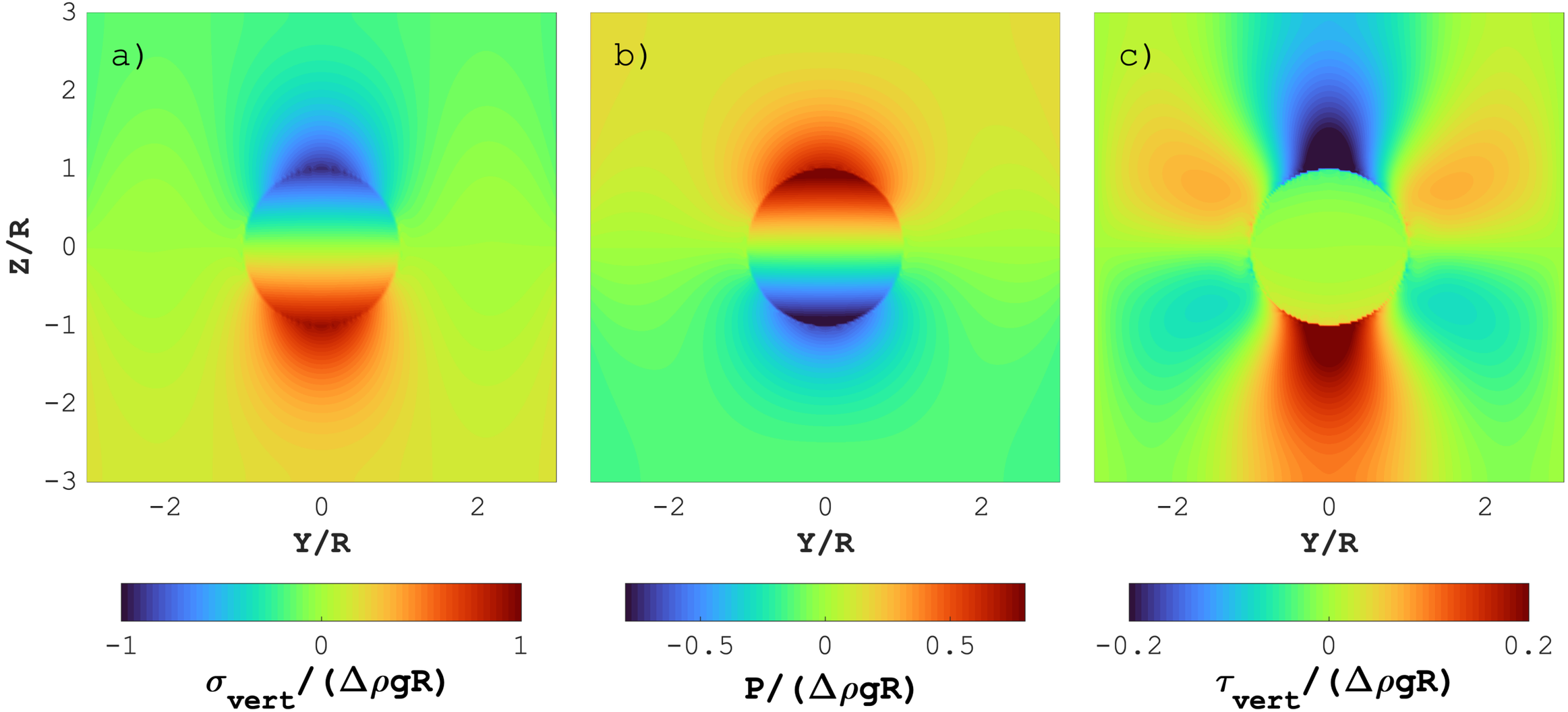
a)
b)
c)
Z/R
3
2
1
0
−1
−2
−3
−2
0
2
Y/R
−1
0
1
$\sigma_{vert}/(\Delta\rho gR)$
−0.5
0
0.5
P/(ΔρgR)
−0.2
0
0.2
$\tau_{vert}/(\Delta\rho gR)$

Figure 5.

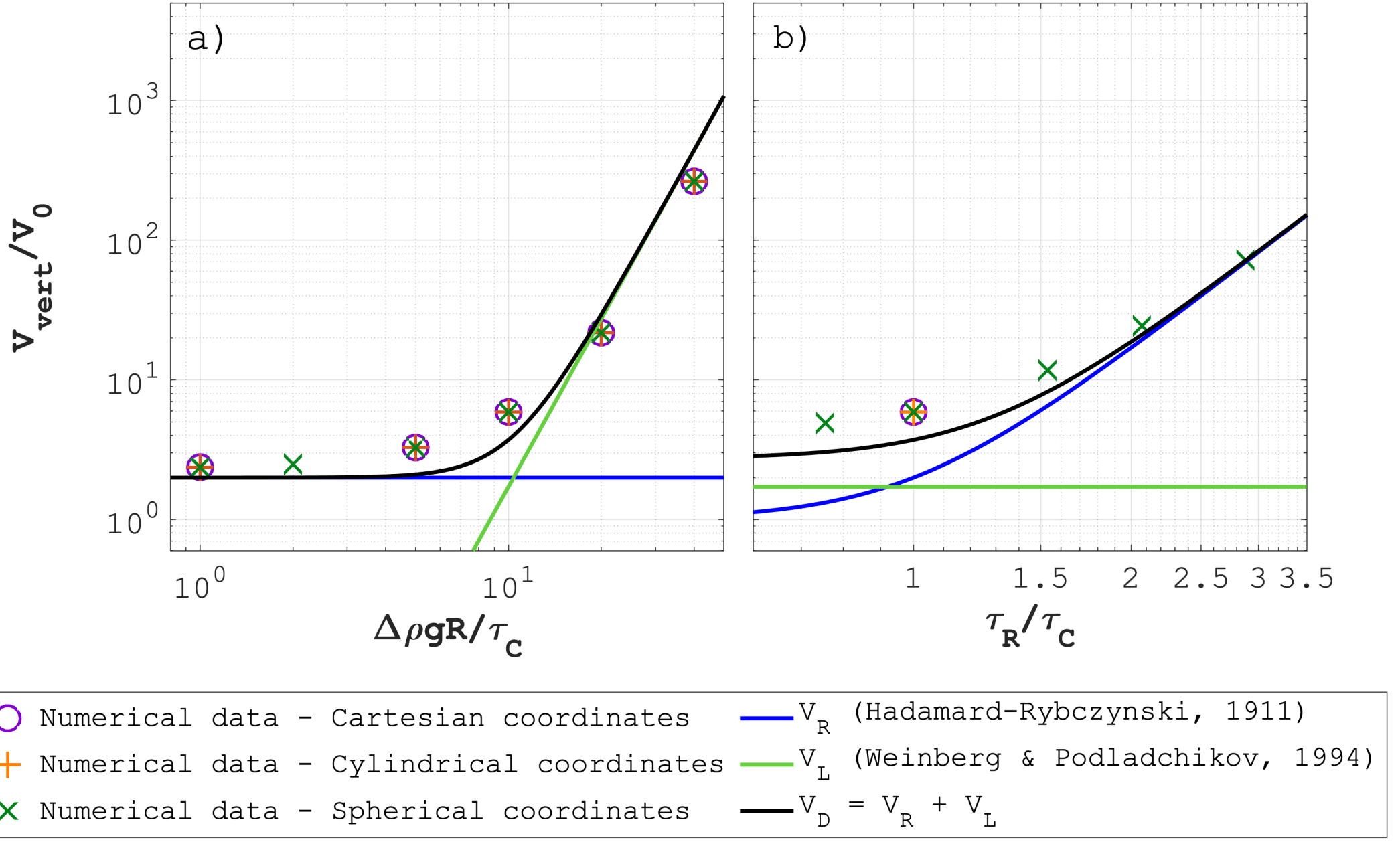
a)
b)
v_{vert}/v_0
10^3
10^2
10^1
10^0
10^0
10^1
$\Delta\rho gR/\tau_C$
1
1.5
2
2.5
3
3.5
τ_R/τ_C
Numerical data - Cartesian coordinates
Numerical data - Cylindrical coordinates
Numerical data - Spherical coordinates
V_R (Hadamard-Rybczynski, 1911)
V_L (Weinberg & Podladchikov, 1994)
$V_D = V_R + V_L$

Figure 6.

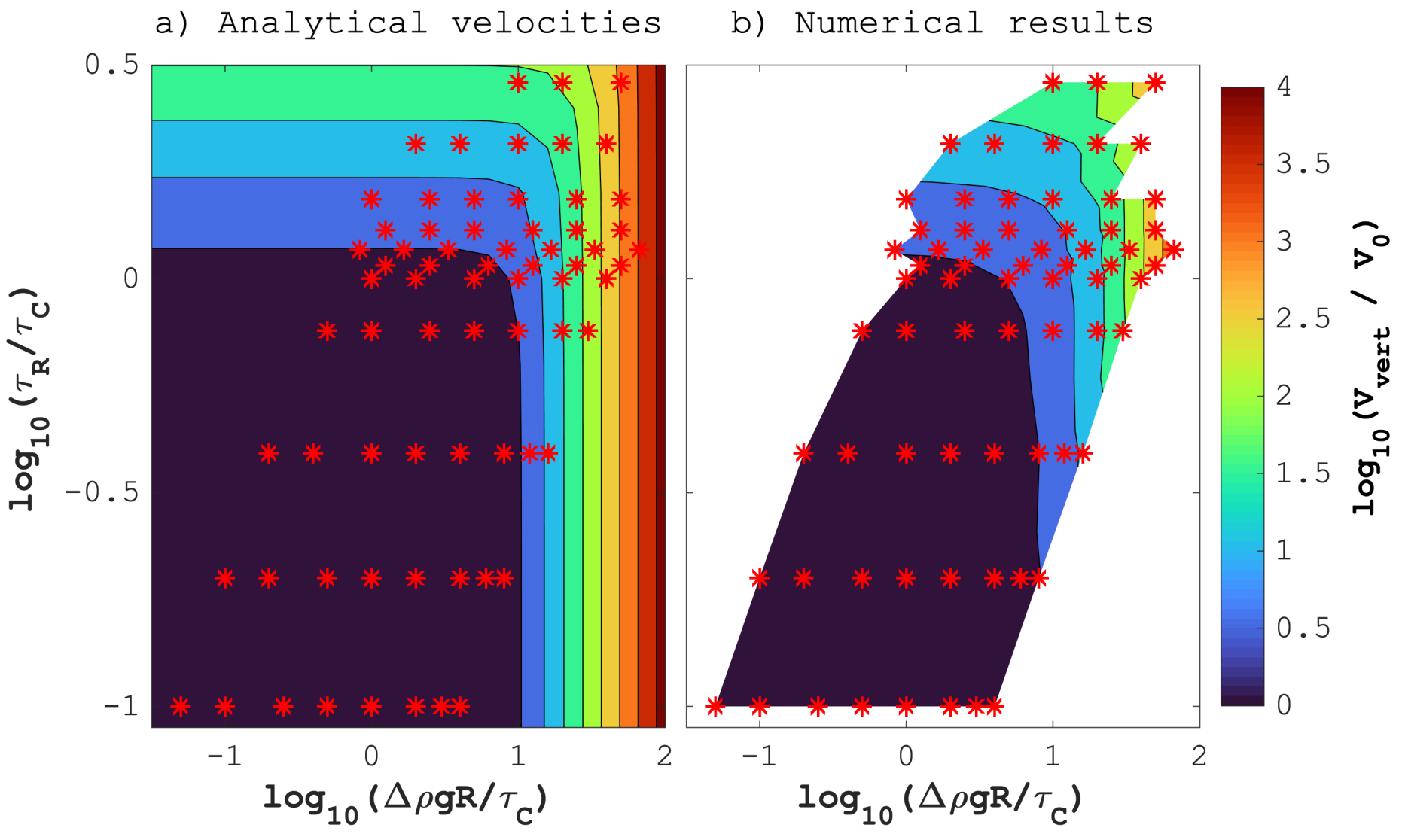
a) Analytical velocities
b) Numerical results
0.5
0
-0.5
-1
log10(τR/τC)
-1
0
1
2
log10(ΔρgR/τC)
4
3.5
3
2.5
2
1.5
1
0.5
0
log10(Vvert / V0)

Figure 7.

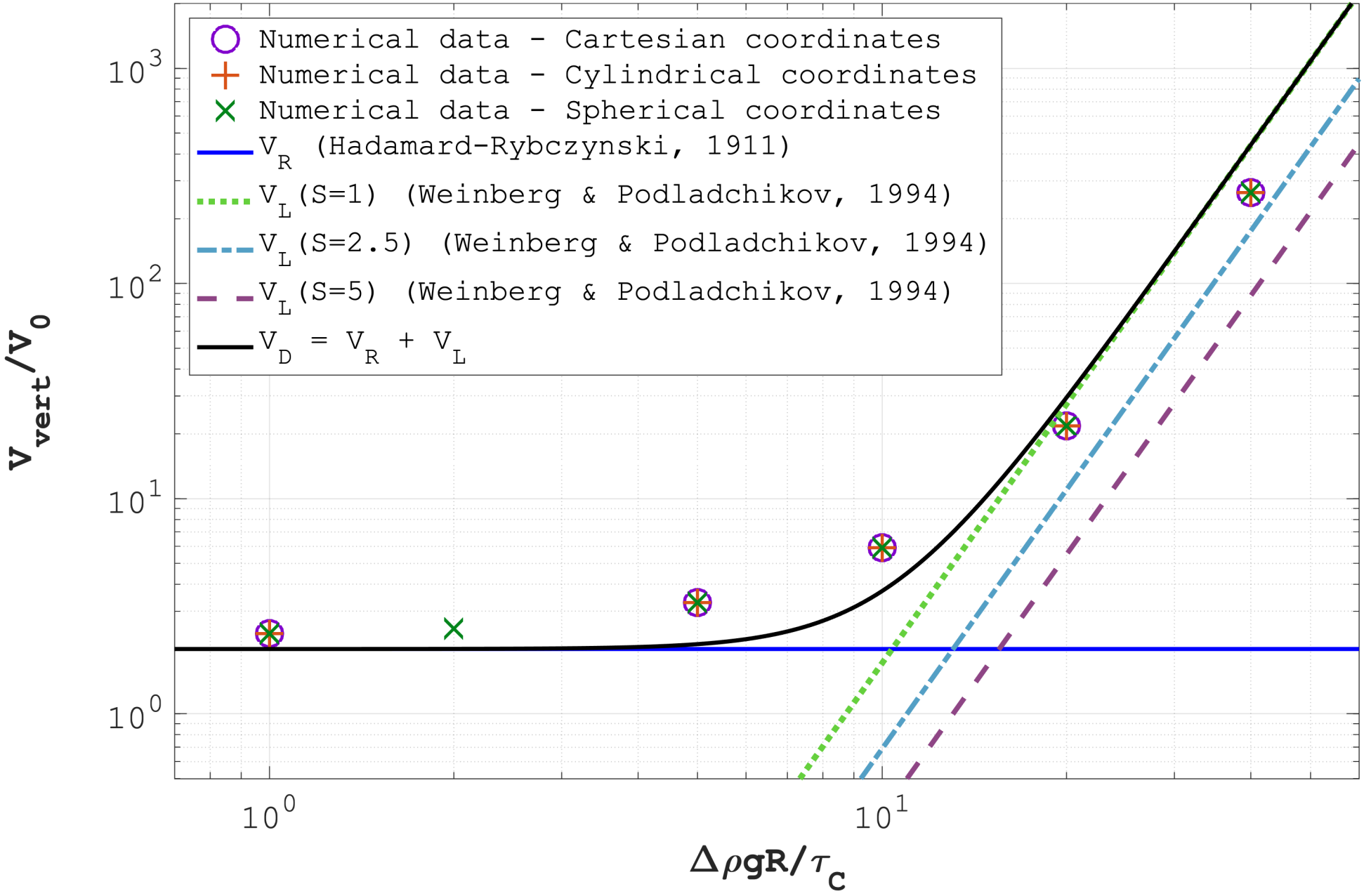
Numerical data - Cartesian coordinates
Numerical data - Cylindrical coordinates
Numerical data - Spherical coordinates
V_R (Hadamard-Rybczynski, 1911)
V_L(S=1) (Weinberg & Podladchikov, 1994)
V_L(S=2.5) (Weinberg & Podladchikov, 1994)
V_L(S=5) (Weinberg & Podladchikov, 1994)
V_D = V_R + V_L
10^3
10^2
10^1
10^0
10^0
10^1
V_vert/V_0
Δρ gR/τ_c

Figure 8.

a) S = 1

b) S = 2.5

c) S = 5

$\log_{10}(V_{vert}/V_0)$

$\log_{10}(V_D/V_0)$

Systematic simulations

Equivalence line

d) Error for different shape factors

$\text{mean}((|V_{vert}-V_D|)/V_{vert})$

S

Error

Minimum error

Figure 9.

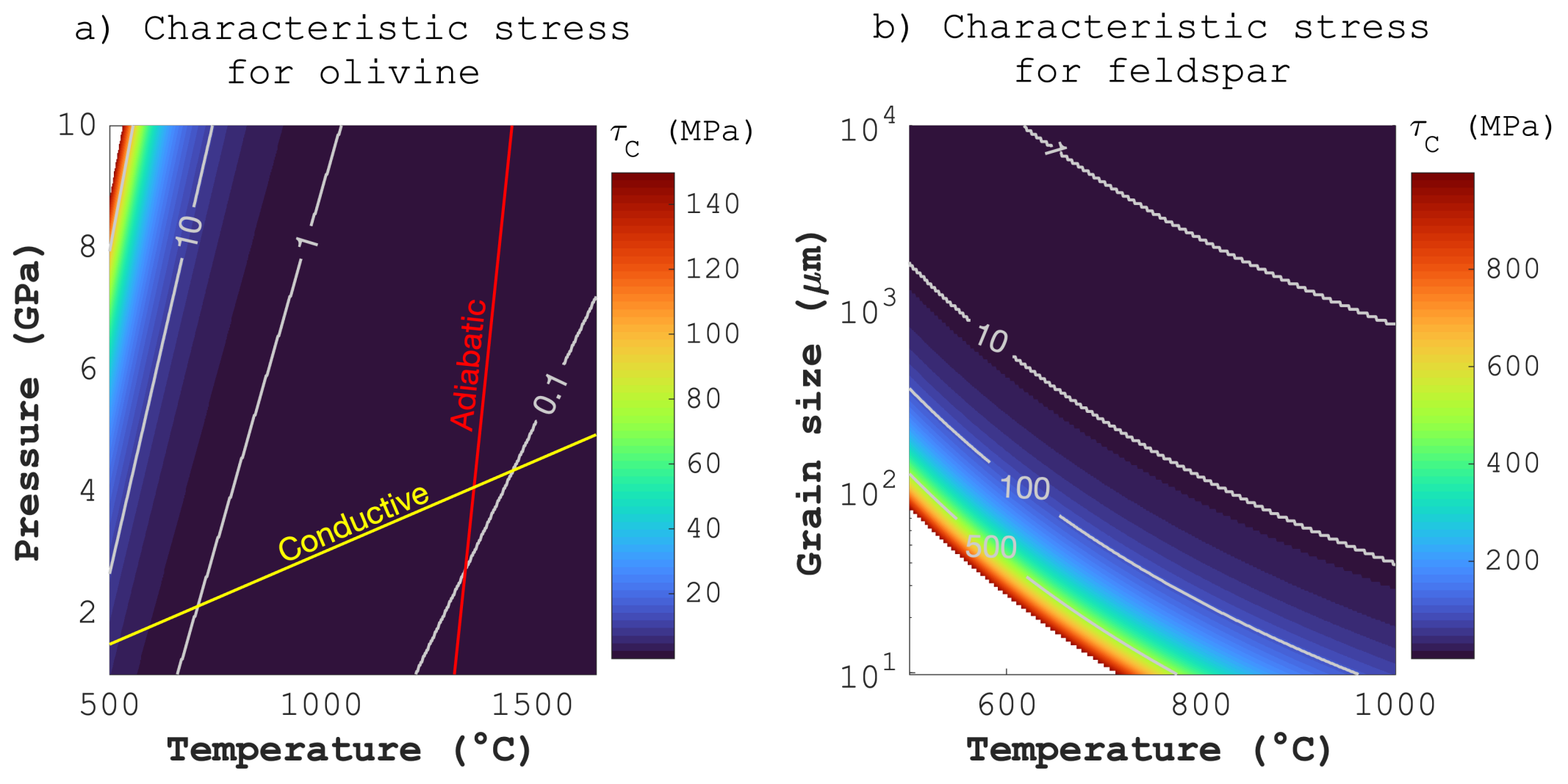
a) Characteristic stress for olivine
b) Characteristic stress for feldspar
Pressure (GPa)
Temperature (°C)
Grain size (μm)
Temperature (°C)
τC (MPa)
τC (MPa)
10
1
0.1
Adiabatic
Conductive
100
500
10
8
6
4
2
500
1000
1500
10^4
10^3
10^2
10^1
600
800
1000
140
120
100
80
60
40
20
800
600
400
200

Figure 10.

a) Analytical velocities (n = 3, Ω = 100)

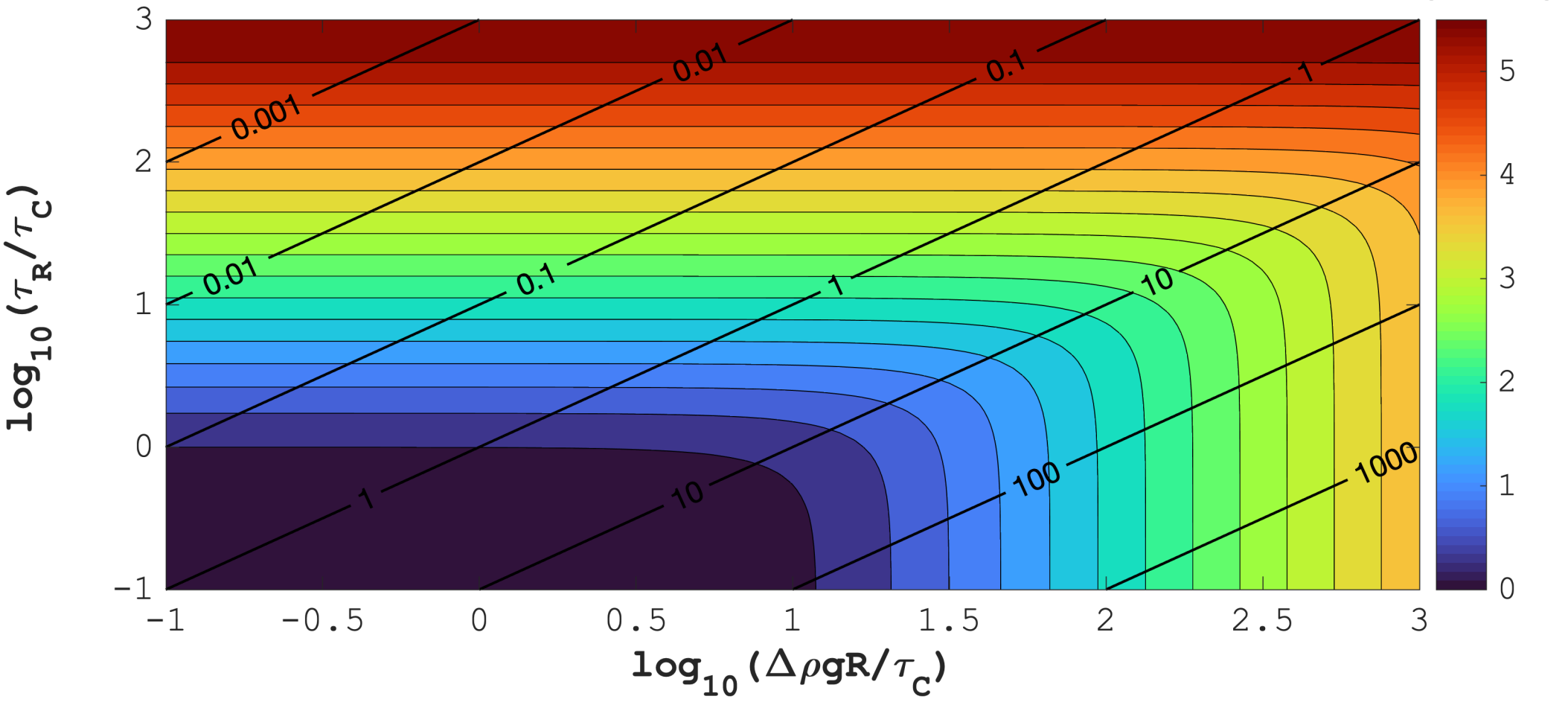

b) Analytical velocities (n = 3, Ω = 100, Δρg = 2000Pa/m, τ_C = 1MPa)

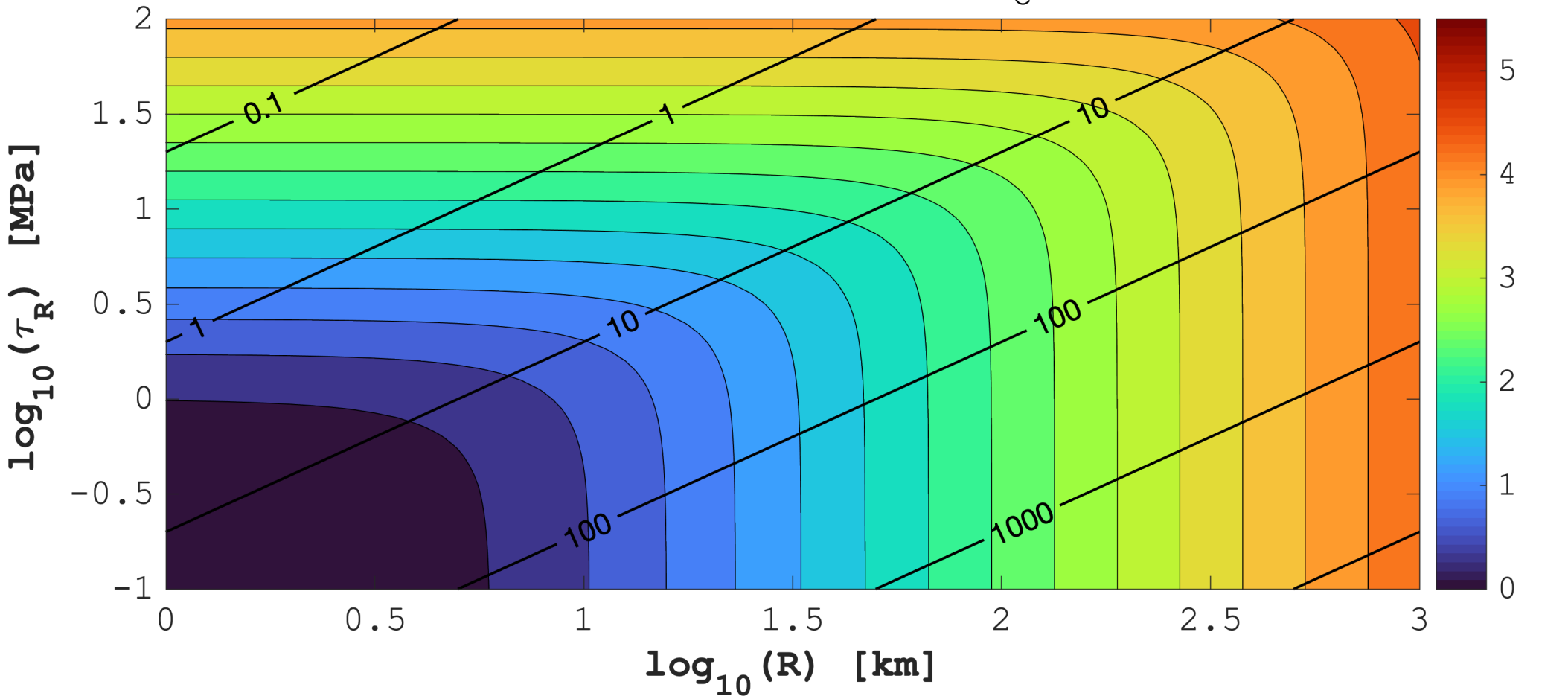

Figure 11.

τ_R = 10MPa,
τ_C = 10MPa

$\Delta\rho$ = 200kg/m^3

$\Delta\rho$ = 20kg/m^3

a)
Sediment diapirs
(U)HP Units

b)
Mantle plumes
(U)HP Units

c)
Sediment diapirs
(U)HP Units

d)
Mantle plumes
(U)HP Units

Velocity [cm/yr]

10^5
10^0
10^{-5}

10^{-1} 10^0 10^1 10^2

Radius [km]

10^0 10^1 10^2 10^3

Radius [km]

10^{-1} 10^0 10^1

Argand number [ ]

10^{-1} 10^0 10^1

Argand number [ ]

η_m [Pas]

1e+17 1e+19 1e+21 1e+23

Critical pluton velocity

Magma plutons

Figure C1.

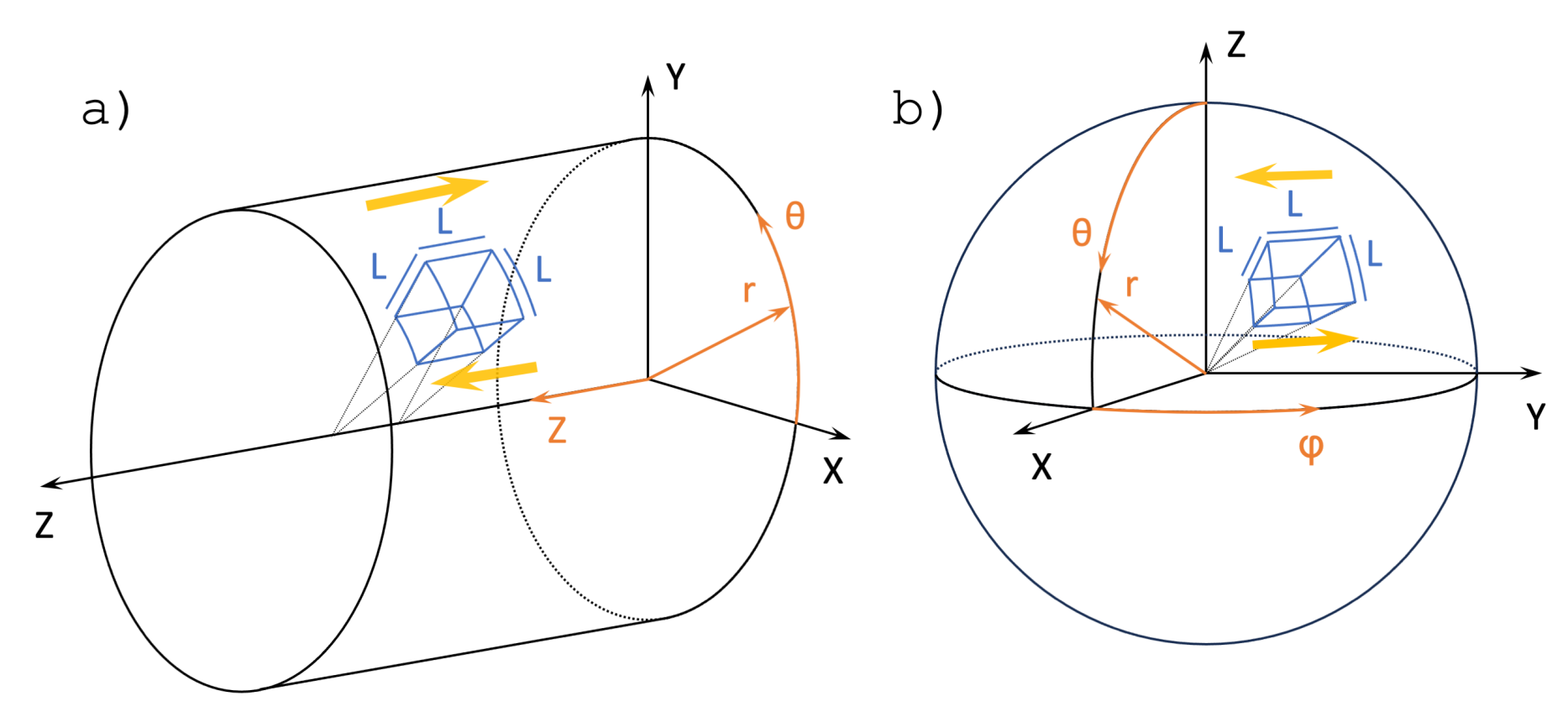
a)
Y
θ
r
L
L
L
Z
X
Z
b)
Z
θ
r
L
L
L
Y
X
φ

Figure C2.

Cartesian

Cylindrical

Spherical

a)

b)

c)

d)

e)

f)

g)

h)

i)

Z/R

r/R

Y/R

θ/R

$\sigma_{vert} / (\Delta\rho gR)$

P/(ΔρgR)

$\tau_{vert} / (\Delta\rho gR)$

Figure D1.

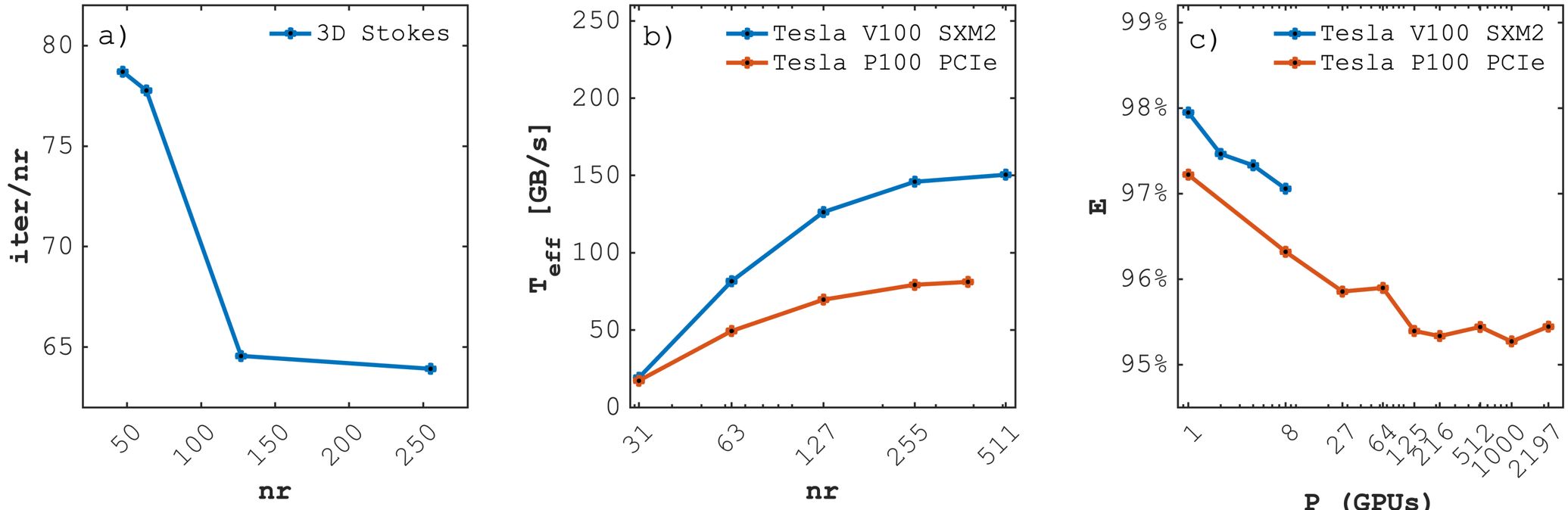
a)
3D Stokes
iter/nr
80
75
70
65
50
100
150
200
250
nr
b)
Tesla V100 SXM2
Tesla P100 PCIe
T_eff [GB/s]
250
200
150
100
50
0
31
63
127
255
511
nr
c)
Tesla V100 SXM2
Tesla P100 PCIe
E
99%
98%
97%
96%
95%
1
8
27
64
125
216
512
1000
2197
P (GPUs)

Figure D2.

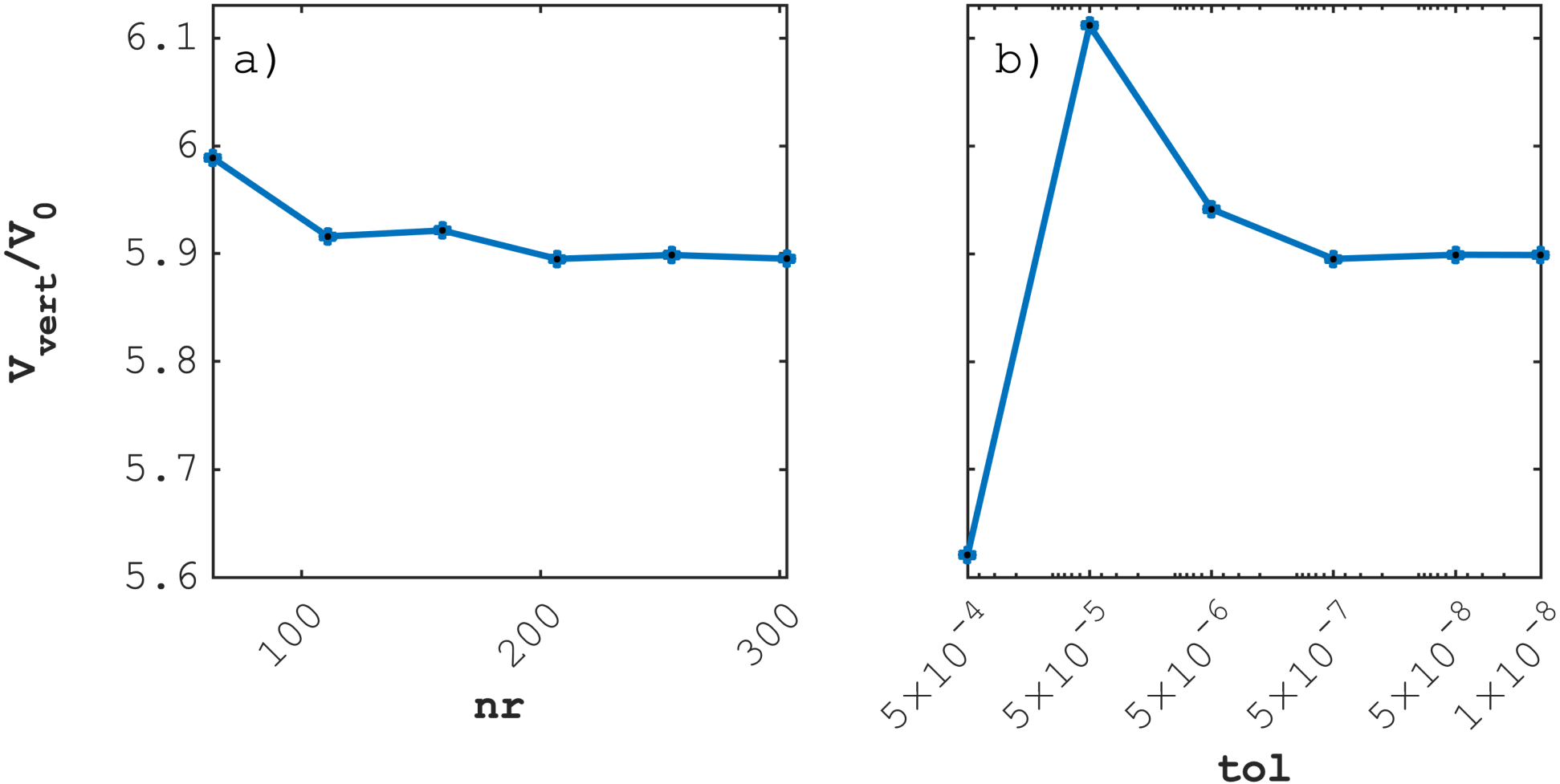
a)
b)
v_{vert}/v_0
6.1
6
5.9
5.8
5.7
5.6
100
200
300
nr
5×10^{-4}
5×10^{-5}
5×10^{-6}
5×10^{-7}
5×10^{-8}
1×10^{-8}
tol